Numerical Analysis of Multirotor Aerodynamic Interactions in Forward and Transition Flight

Kangni Combey,*,† Omer A. Elsayed,‡ Khaoula Qaissi,§ Hajar Chouiyakh,§ and Faqir Mustapha¶
International University of Rabat, Sala Al Jadida 11100, Morocco

https://doi.org/10.2514/1.C038518

The growing demand for urban air mobility (UAM) has accelerated the development of hybrid/electric vertical takeoff and landing (H-/eVTOL) aircraft, which use distributed propulsion systems that generate complex aerodynamic interactions during forward and transition flight. This study investigates the aerodynamic interactions between two propellers arranged in a one-after-another (OAA) configuration, using unsteady Reynolds-averaged Navier–Stokes (URANS) simulations coupled with the k-ω shear stress transport (SST) turbulence model. The numerical setup was validated against experimental data for the isolated propeller across all investigated advance ratios, showing good agreement. Results reveal that, in forward flight, the rear propeller experiences up to 24% thrust and 20% power loss due to the disturbed airflow created by the wake of the front propeller. This is accompanied by only a 21% increase in axial velocity at the rear propeller location, indicating less effective energy transfer and lower thrust. Pressure coefficient analysis at the rear propeller midspan within the overlap region indicates increased flow separation and lower local loading. During transition, the overlap decreases with tilt, yet at 30° and 60°, the rear propeller still loses up to 11% thrust and 10% power due to slipstream deflection. As the propeller tilt angle increases, the thrust in the propeller axis direction also increases; however, this requires more power and generates a more complex slipstream. These findings provide valuable insights into wake interactions and their influence on rear propeller performance, offering practical design guidelines to improve the efficiency and reliability of UAM vehicles.

Nomenclature

C_p	=	pressure coefficient, $(p - p_\infty)/(0.5\rho_\infty V_{R_\infty}^2)$
C_P	=	power coefficient, $P/(\rho_\infty n^3 D_p^5)$
C_Q	=	torque coefficient, $Q/(\rho_\infty n^2 D_p^5)$
C_T	=	thrust coefficient, $T/(\rho_\infty n^2 D_p^4)$
DEP	=	distributed electric propulsion
D_p, R_p	=	propeller diameter and radius, m
eVTOL	=	electric vertical takeoff and landing
FB	=	front propeller blade
H-VTOL	=	hybrid vertical takeoff and landing
ISO	=	isolated propeller
J	=	advance ratio, $J = (V_\infty/nD_p)$
n	=	propeller revolutions per second, rev/s
N_{rev}	=	number of propeller revolutions
u	=	axial velocity, m/s
OAA	=	one-after-another
RB	=	rear propeller blade
RD	=	rotating domain
SD	=	surrounding domain
TE	=	trailing edge
UAM	=	urban air mobility
V_∞	=	freestream velocity, m/s
α_p	=	propeller angle, deg
ρ_∞	=	freestream density, kg/m^3
Ψ	=	azimuthal angle, deg

Subscripts

front	=	front propeller
rear	=	rear propeller
∞	=	freestream condition

I. Introduction

THE concept of urban air mobility (UAM) represents an exciting shift in urban transport, leveraging advanced aeronautical technologies such as hybrid/electric vertical takeoff and landing (H − /eVTOL) aircraft driven by distributed electric propulsion systems. UAM envisions a future where eVTOL and H-VTOL aircraft are easily integrated into urban airspace, offering a novel mode of transportation for both intercity and intracity travel that promises to alleviate ground congestion, reduce travel times, and increase accessibility to previously hard-to-reach locations such as remote mountains [1–3]. These aircraft have the potential to transform the transportation ecosystem into a more sustainable one [4]. This shift is crucial to achieve carbon neutrality in the transport sector. In addition, UAM promises to provide a diverse array of services, ranging from emergency transportation to delivery services. Cities can improve their emergency response capabilities and accelerate service delivery by using the agility and versatility of eVTOL aircraft.

These vehicles are characterized by distributed electric propulsion (DEP) and distributed hybrid propulsion systems with low-disk loading rotors. They have predominantly adopted propeller-driven propulsion systems, mainly due to their operation within the relatively low-altitude airspace of urban environments, typically below 1200 m [5]. At these lower altitudes, propeller-driven systems are recognized for their superior efficiency [6], and rotating blades produce lift, which is required to propel the aircraft into the air [7]. The DEP system plays a pivotal role in facilitating the efficient development of eVTOL aircraft. In contrast to single larger rotor vehicles, for instance a helicopter, DEP technology contributes to a reduction in overall aircraft noise while simultaneously offering enhanced efficiency

Received 19 April 2025; accepted for publication 10 August 2025; published online 9 September 2025.

*Ph.D. Researcher, School of Aerospace and Automotive Engineering; kangni.combey001@gmail.com. Member AIAA.

†Visiting Ph.D. Researcher, Flow Physics and Technology Department, Faculty of Aerospace Engineering, Delft University of Technology, 2629 HS Delft, The Netherlands; k.combey@tudelft.nl.

‡Associate Professor, School of Aerospace and Automotive Engineering; omer.almatbagi@uir.ac.ma.

§Assistant Professor, School of Aerospace and Automotive Engineering.

¶Full Professor, Dean, School of Aerospace and Automotive Engineering.

[4]. This is primarily attributed to the utilization of smaller rotors, which not only demand less power for lift but also prove to be well suited for the unique requirements of eVTOL operations. Moreover, the use of smaller rotor blades in DEP configurations presents distinct advantages in urban environments. These smaller rotors are less prone to damage upon contact with the infrastructure than larger ones, thus enhancing safety and operational reliability. Furthermore, the inherent redundancy provided by multirotor designs ensures greater stability, even in the event of a motor failure [8]. Furthermore, the ability to independently control each rotor enables precise pose control, a task that is inherently more challenging with single-rotor configurations.

Different concepts have been proposed with multiple propellers, which are mounted on lifting surfaces, as shown in Figs. 1a and 1b, or on nonlifting arms, as shown in Fig. 1c.

Johnson et al. [9] and Silva et al. [10] have presented various concepts of eVTOL aircraft featuring different propeller layouts as reference models for the development of technologies. These authors emphasize performance considerations arising from the rotor–rotor interaction. The interaction among multiple rotors can significantly influence vehicle performance. Although the DEP system offers distinct advantages, it is imperative to consider the resulting interactions between the propellers during the conceptual design phase.

Aerodynamic interactions between rotors have been extensively investigated in the literature, particularly with regard to helicopters [11–13]. However, the findings of rotorcraft research may not be immediately applicable to the aerodynamic interactions observed in multirotor eVTOL aircraft configurations, since both operate with different mechanisms and flow regimes [14].

Recent research has delved extensively into the aerodynamic interactions between eVTOL propellers in various configurations. Studies have demonstrated that when propellers are placed in close proximity to each other, there is a notable impact on rotor performance. This proximity often leads to unsteady loading on the propeller blades [15–17] and a reduction in thrust produced at a given rotational speed, typically ranging from 2 to 80%, depending on the specific configuration [15–21]. Consequently, the efficiency of the system decreases.

De Vries et al. [22] analyzed the aerodynamics of a side-by-side (SBS) configuration of a three-propeller setup, identifying efficiency losses driven by the influence of adjacent propellers on the middle one. They found that differential thrust alters the inflow conditions and blade loading, causing local disk loading variations of 5–10%. These results were later corroborated by Gao et al. [23]. Piccinini et al. [24] observed slight performance losses in SBS configurations but more significant reductions in OAA configurations, particularly at smaller lateral distances. The fully overlapping configurations resulted in 30% thrust loss and 20% efficiency loss due to increased advance ratio effects.

Stokkermans [18] found that fully overlapping propellers experience up to 80% thrust loss due to nonuniform inflow and wake ingestion and that thrust and power coefficients depend strongly on lateral spacing, driven by slipstream impingement. Similarly, Combey et al. [25] reported a 12% thrust reduction for the rear propeller in OAA configuration with a hub spacing of $1.4R_p$ compared to the front propeller.

Analysis of the influence of close-proximity rotors on aerodynamic performance has shown that in one-after-another (OAA) configurations, the lateral spacing between rotors should be at least equal to the propeller diameter ($d_y = 2R_p$) to limit thrust reduction on the rear rotor to below 4%. In contrast, side-by-side (SBS) configurations exhibit minimal overall performance impact, with thrust differences less than 3%, suggesting no significant disadvantages to employing distributed electric propulsion in such arrangements. However, inherent fluctuations in these configurations may lead to additional challenges, such as increased noise generation. These observations highlight the importance of accurately assessing aerodynamic interactions during the design phase.

To address these challenges, a different approach can be used, including advanced flow control techniques. This method has shown significant potential to improve the aerodynamic performance of propulsion systems. Active and passive flow control devices play a crucial role in preventing or delaying flow separation, mitigating turbulence, reducing wake intensity, or redirecting wake flow downstream. Numerous studies have shown the efficacy of employing these flow control strategies [26–29].

Among the multirotor concepts proposed for UAM, the tilt-wing and tilt-rotor configurations are notable for their vectored thrust capabilities. In tilt-wing configurations, the wing and attached propellers tilt as a single unit, whereas in tilt-rotor configurations, only the rotors are tilted with the wing remaining fixed. These systems enable the aircraft to transition between vertical and horizontal flight by varying the tilt angle, also denoted in this study as the propeller angle α_p, which ranges from 0° (horizontal orientation) to 90° (vertical orientation) and vice versa. The introduction of a vectored thrust design adds more complexity, extending the challenges associated with multirotor interactions.

Although substantial research has focused on aerodynamic interactions during hover and forward flight phases, vectored thrust eVTOL aircraft, a key technology in urban air mobility, present unique challenges, particularly during the transition phase. This phase, where the aircraft shifts between vertical and horizontal flight, introduces complex flow dynamics that require detailed investigation for the continued development of these vehicles. Previous studies by Stokkermans et al. [18] and Zanotti et al. [30] investigated aerodynamic interactions during transition flight for specific positions. Their focus was on experimentally measuring average performance characteristics rather than analyzing wake dynamics.

The aim of this study is to numerically investigate the aerodynamic behavior of propellers in an OAA configuration during forward flight and the transition phase, with a particular focus on wake interactions and their impact on performance. Simulations are conducted to analyze the flow characteristics across a range of rotor tilt angles—from horizontal (forward flight) to vertical (edgewise flow), representing the full operational envelope of tiltrotor eVTOL configurations. This work is based on the numerical method, which provides a cost-effective and versatile tool for capturing complex aerodynamic phenomena. Through this approach, the study offers critical insights into multirotor aerodynamic interactions during the

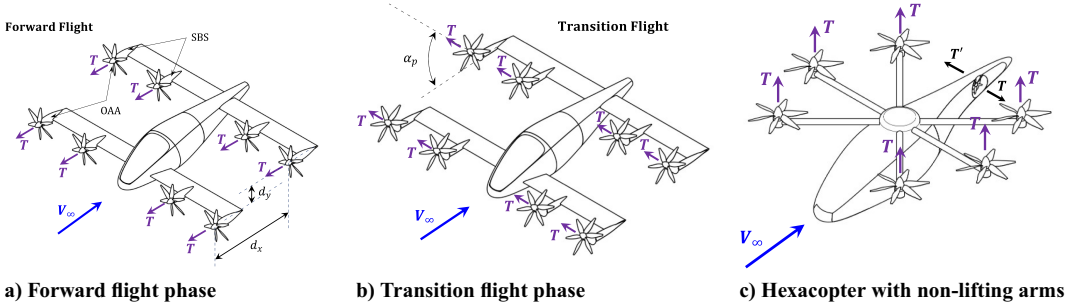

a) Forward flight phase b) Transition flight phase c) Hexacopter with non-lifting arms

Fig. 1 Multirotor eVTOL vehicle concepts with tilt-rotors, showing propellers in SBS and OAA configurations and on Hexacopter arms.

transition phase, with the ultimate goal of supporting the efficient design of UAM eVTOL aircraft.

II. Methodology

A. Geometry and Configurations

The TUD-F29 four-bladed propeller, with a diameter of $D_p = 0.3048$ m and a blade pitch of $\beta_{0.7R_p} = 20°$ (see Fig. 2), was used in this study.

The radius of the hub is $R_h = 0.28R_p$. The F29 propeller has been used for the numerical study focusing on the aerodynamics of the propeller and the interaction between the propellers in the OAA configuration during the forward and transition phases. Its selection was based on the need for coherence in validating the numerical setup with the experimental results presented by Stokkermans et al. [18]. The geometrical specifications of the F29 propeller blade, accompanied by airfoil data, are freely available in the open-source literature by the authors [18]. Two propellers in an OAA configuration were considered.

To establish a baseline for comparison, an isolated propeller was first analyzed in horizontal flight conditions, as illustrated in Fig. 3a. Subsequently, as shown in Figs. 3b–3d, two propellers were placed in the OAA configuration with a lateral spacing of $d_y = R_p$ and a longitudinal spacing of $d_x = 2.5R_p$. These spacings are defined in a fixed reference frame and remain constant as the propellers rotate. The selected spacing values provide a configuration that ensures clear observation of propeller–propeller interaction effects, without direct overlap of the wakes. The OAA configuration was evaluated under the same conditions as the isolated propeller to ensure consistency. A summary of all test cases is provided in Table 1.

B. Computational Domain and Boundary Conditions

To accurately simulate the rotational motion of the propeller, two computational flow domains were defined: a rotating domain (RD) surrounding the blades and a stationary domain (SD) representing the surrounding flowfield (see Fig. 4). The interface between the rotating and stationary domains was modeled using a sliding mesh interface (mesh motion), which allows for the continuous and conservative transfer of flow variables across the rotating and stationary regions. To effectively capture wake dynamics and maintain appropriate far-boundary and freestream conditions, the SD dimensions were adapted for each transition angle, as detailed in Table 2. Figure 4b illustrates the geometric definition of the stationary domain extents around the rotating domains. The inlet boundary condition was defined as a velocity inlet with a uniform freestream velocity of $V_\infty = 20$ m/s, while the outlet was defined as a pressure outlet with a static gauge pressure of 0 Pa.

All other SD boundaries were treated as far-field boundaries with zero shear stress. The propeller surfaces were modeled as no-slip walls to ensure an accurate representation of the effects of the boundary layer and the interaction between the blade and the flow.

C. Mesh Generation and Mesh Independence

Unstructured tetrahedral mesh was generated using ANSYS Meshing, with grid density controlled through face sizing and volume refinement. The propeller blades were surrounded by 20 inflation layers with a growth rate of 1.2 and a thickness of the first layer that corresponds to $y+ = 0.8$.

A mesh independence study was conducted, and the results showed minor variations in aerodynamic coefficients with higher mesh resolution. Specifically, the thrust coefficient (C_T) changed by only 0.07%

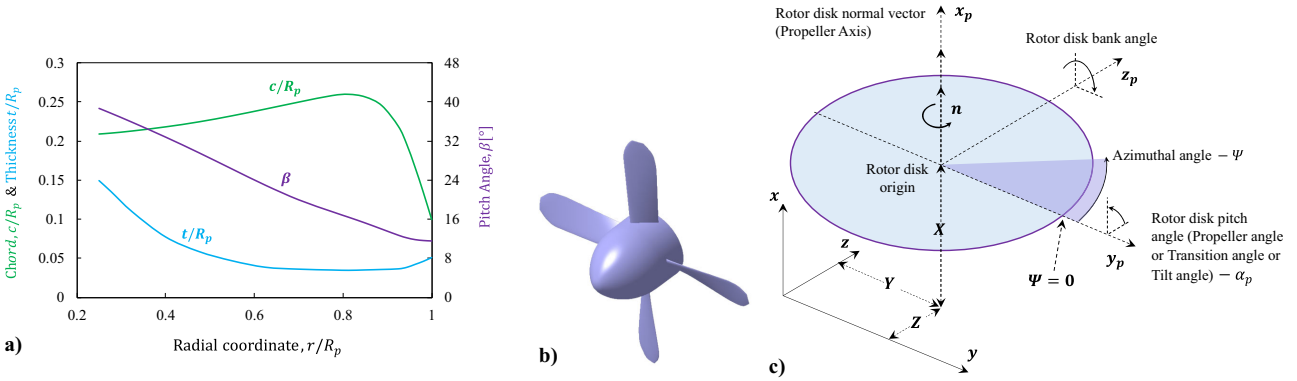

Fig. 2 F29 propeller: a) blade characteristics in radial direction, b) propeller geometry, and c) rotor disk schematic, angles, and axes definition.

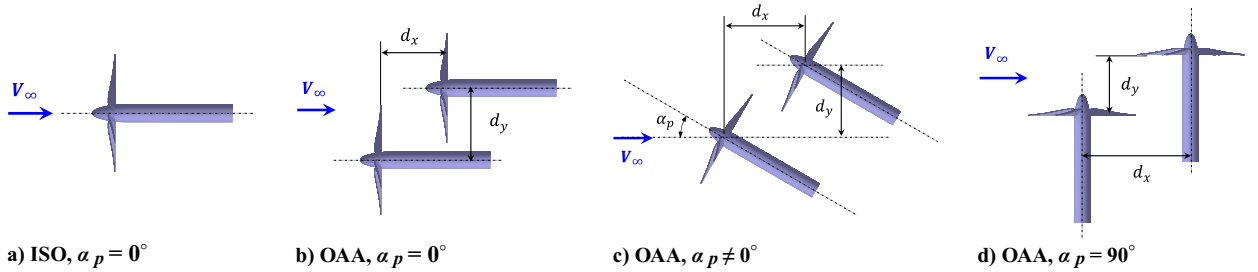

Fig. 3 a) Isolated (ISO) propeller in horizontal flight. Two OAA propellers in b) horizontal, c) transition, and d) vertical flight phases.

Table 1 Summary of considered cases for performance predictions (step of J is 0.2 and α_p is 30°)

Config.	V_∞, m/s	J	n, rev/s	$Re_{c@0.7R_p}$	α_p, °	d_y/R_p	d_x/R_p
ISO	20	[0.2–0.8]	[328–82]	[2.02×10^5–7.89×10^5]	0	— —	— —
OAA	20	[0.2–0.8]	[328–82]	[2.02×10^5–7.89×10^5]	[0–90]	1	2.5

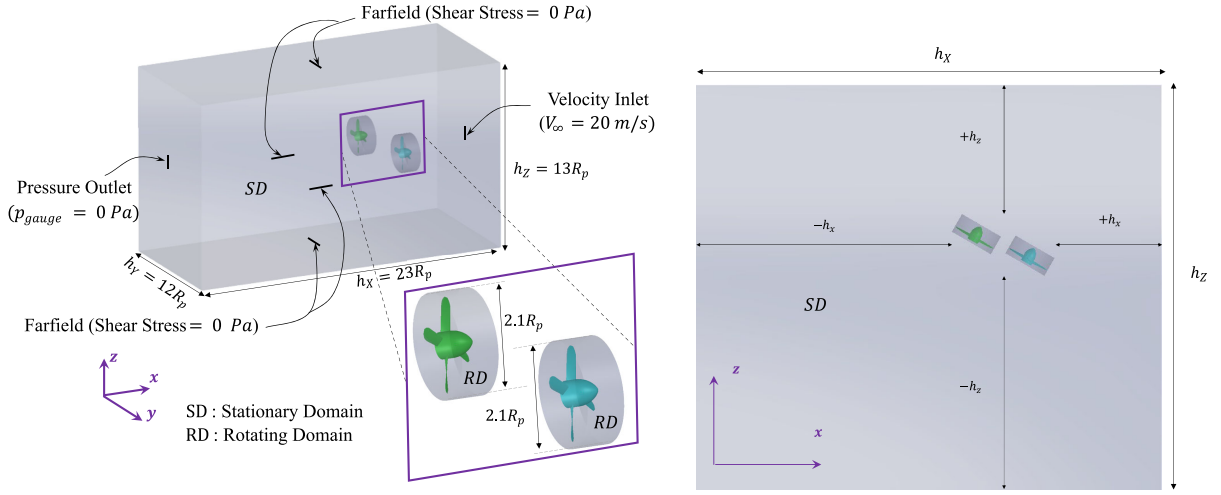

a) α_p = 0°, isometric view **b) α_p = 60°, side view**

Fig. 4 Computational domain illustrating the stationary domain (SD) and rotating domain (RD), with specified boundary conditions: velocity inlet, pressure outlet, and zero-shear wall far field.

Table 2 Summary of stationary domain dimensions around the rotating domains

α_p, °	$-h_x/R_p$	$+h_x/R_p$	$-h_y/R_p$	$+h_y/R_p$	$-h_z/R_p$	$+h_z/R_p$
0	15	5	5	5	5	5
30	15	5	5	5	5	5
60	12	5	5	5	10	6
90	10	5	5	5	10	6

when the mesh size increased from 8.6 to 12.9 million elements, while the torque coefficient (C_Q) varied by just 0.02% (see Fig. 5). Based on these results, a mesh resolution of 8.6 million elements was found to be sufficient to accurately capture the aerodynamic characteristics while maintaining a reasonable computational cost. Figure 6 illustrates the final mesh configuration, showing the surface mesh on the blades and the inflation layers around a representative blade section. The same mesh setup was applied for all configurations.

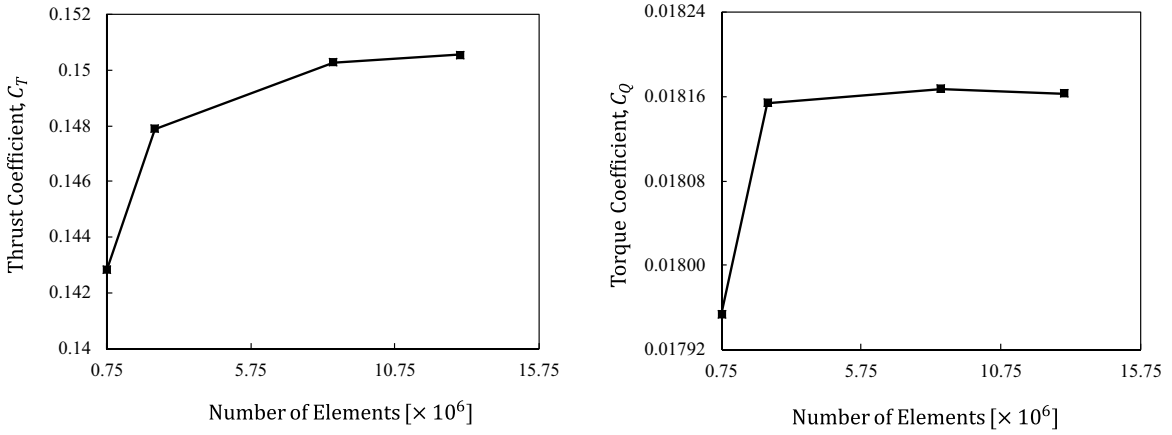

a) Thrust coefficient, C_T **b) Torque coefficient, C_Q**

Fig. 5 Mesh independence study for the isolated propeller: a) thrust coefficient C_T and b) torque coefficient C_Q.

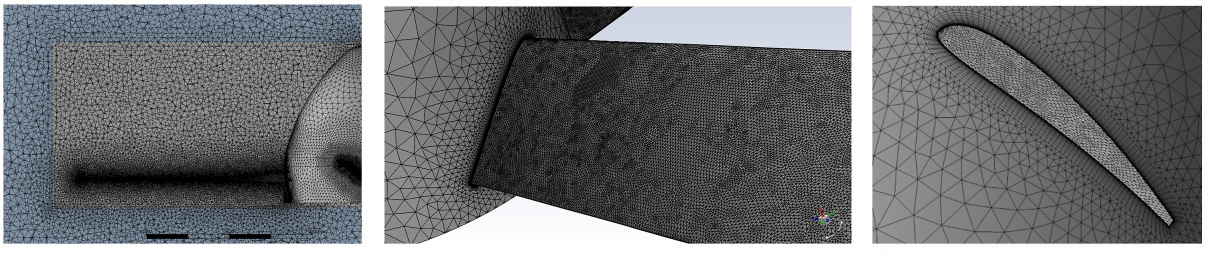

a) **b)** **c)**

Fig. 6 Computational mesh showing a) mesh refinement near the blade, b) blade surface mesh, and c) inflation layers around the blade section.

D. Governing Equations and Turbulence Model

The motion of a viscous fluid can be described by the following [31]:

Conservation of mass:

$$\frac{\partial \rho}{\partial t} + \nabla(\rho \boldsymbol{v}) = 0 \tag{1}$$

where ρ is the density and $\boldsymbol{v}$ is the velocity.

Conservation of momentum:

$$\overbrace{\frac{\partial}{\partial t}(\rho \boldsymbol{v})}^{\text{I}} + \overbrace{\nabla \cdot (\rho \boldsymbol{v}\boldsymbol{v})}^{\text{II}} = \overbrace{-\nabla p}^{\text{III}} + \overbrace{\nabla \cdot (\bar{\bar{\tau}})}^{\text{IV}} \tag{2}$$

where I is the local change with time, II is momentum convection, III is surface force, and IV is the diffusion term, and $\bar{\bar{\tau}}$ is the viscous stress tensor.

Conservation of energy:

$$\frac{\partial}{\partial t}(\rho E) + \nabla \cdot (\boldsymbol{v}(\rho E + p)) = \nabla \cdot \left(k_{\text{eff}} \nabla T - \sum_j h_j \boldsymbol{J}_j + (\bar{\bar{\tau}}_{\text{eff}} \cdot \boldsymbol{v}) \right) \tag{3}$$

where k_{eff} is the effective conductivity, $\boldsymbol{J}_j$ is the diffusion flux of species j, and E is the energy of the system.

In the k-ω shear stress transport (SST) model, the turbulence kinetic energy k and the specific dissipation rate ω are obtained from Eqs. (4) and (5):

$$\frac{\partial}{\partial t}(\rho k) + \frac{\partial}{\partial x_i}(\rho k u_i) = \frac{\partial}{\partial x_j}\left(\Gamma_k \frac{\partial k}{\partial x_j} \right) + \tilde{G}_k - Y_k \tag{4}$$

$$\frac{\partial}{\partial t}(\rho \omega) + \frac{\partial}{\partial x_i}(\rho \omega u_i) = \frac{\partial}{\partial x_j}\left(\Gamma_\omega \frac{\partial \omega}{\partial x_j} \right) + G_\omega - Y_\omega + D_\omega \tag{5}$$

where $\tilde{G}_k$ and G_ω denote the turbulence kinetic energy and specific dissipation rate, respectively. Γ_k and $\Gamma\omega$ represent their effective diffusivities, while Y_k and Y_ω are their turbulent dissipation, and D_ω represents the cross-diffusion term.

E. Physical Setup

In this study, the effects of turbulence were accounted for using the two-equation k-ω SST turbulence model [32], which is well suited for capturing rotational phenomena, boundary-layer separation, and adverse pressure gradients typical of propeller rotational flows. In the implemented sliding mesh methodology, the cell zones rotate in defined increments relative to each other along the mesh interface while maintaining conservative flux transfer across the mesh interfaces. The time step size was determined based on the propeller geometry and operating conditions, using the following equation, which was derived from previous works by the authors [25]:

$$\Delta t = 1/(nB\Delta d) \tag{6}$$

Here, n is the rotational speed in rev/s, B is the number of blades, and Δd is the number of subdivisions for a single blade passing. This approach enables us to capture the flow characteristics of the propeller. For $\Delta d = 15$, the resulting time step size Δt at $J = 0.4$ is 100 μs, which corresponds to 6° of propeller rotation per time step. This choice provides 60 time steps per revolution, which preliminary studies found sufficient to capture key flow phenomena accurately while ensuring numerical stability and computational efficiency. The simulations are carried out with the propellers at a $V = 20$ m/s flow speed and an advance ratio ranging from 0.2 to 0.8, and in OAA configurations, the two propellers are corotating.

All simulations were run for a minimum of 10 propeller revolutions ($N_{\text{rev}} \geq 10$), with data from the final two revolutions used to eliminate transient startup effects and ensure convergence of the unsteady solution. Time histories of thrust and torque were monitored, and the results were time-averaged over the last two revolutions after full convergence was achieved to obtain representative performance metrics. Figure 7 illustrates the convergence of the thrust coefficient for the front and rear propellers in the OAA configuration at a propeller angle of $\alpha_p = 0°$, with the simulation carried out for $N_{\text{rev}} = 13$ rev olutions. The convergence of C_T for the front propeller, shown in Fig. 7a, indicates that transient startup effects occur during the first two revolutions, with the solution achieving full convergence approximately at the seventh revolution, showing negligible fluctuations. For the rear propeller, shown in Fig. 7b, the start effects persist up to the fourth revolution, and noticeable load fluctuations are observed, characterized by a peak-to-peak variation of $\Delta C_T = 0.036$. These fluctuations show a periodic behavior, with a period corresponding to an azimuthal angle of $\Psi = 90°(N_{\text{rev}} = 0.25)$. The calculated thrust coefficient for the rear propeller is therefore taken as the mean of these oscillations.

The numerical simulations assume uniform freestream inflow, rigid propeller blades with no structural deformation, compressible viscous flow modeled as an ideal gas, and fully turbulent flow resolved using the URANS approach with the k-ω SST turbulence model.

III. Validation of the Numerical Setup

The numerical setup was initially validated against experimental wind tunnel data from Grande et al. [33], using a two-bladed propeller derived from the APC 9 × 6 model, with a radius of $R_p = 0.15$ m, $\beta_{0.75R_p} = 15.8°$, and $c_{\max} = 0.034$ m, operating at a rotational speed of 4000 rpm.

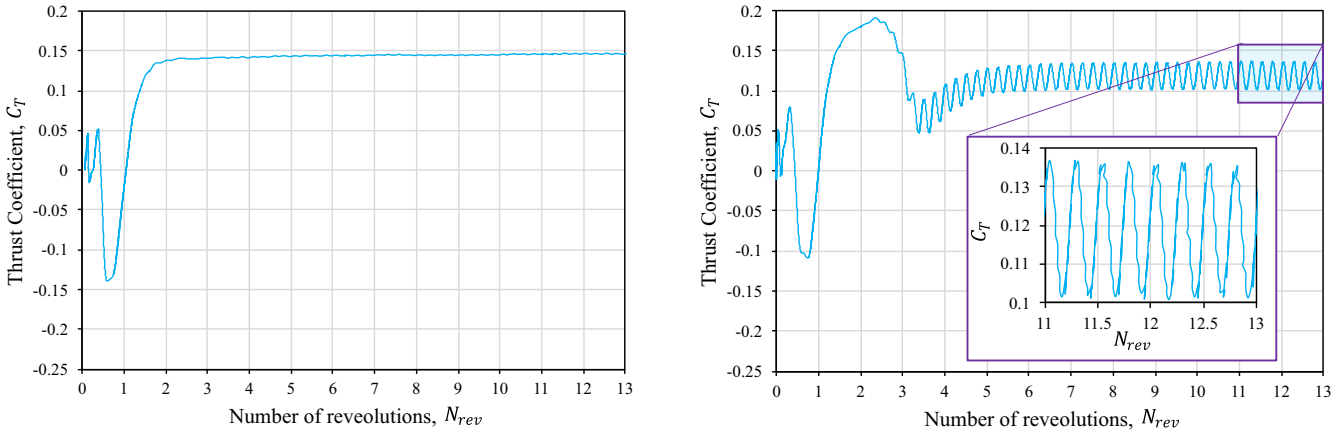

a) Convergence of front propeller thrust coefficient, $C_{T_{front}}$ **b) Convergence of rear propeller thrust coefficient, $C_{T_{rear}}$**

Fig. 7 Convergence of thrust coefficients for front and rear propellers, at $\alpha_p = 0°$ and $J = 0.4$.

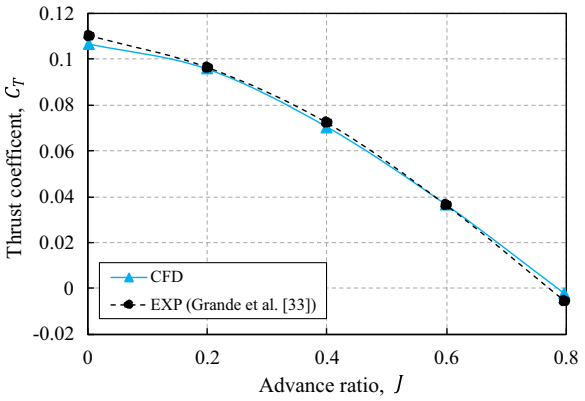

Fig. 8 Comparison of thrust coefficient for isolated propeller: simulation vs experimental data extracted from Grande et al. [33] at $n = 4000$ rpm and $\alpha_p = 0°$.

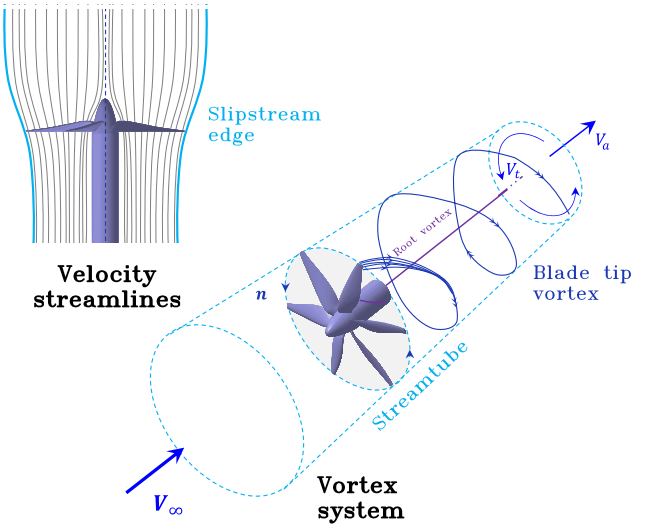

Fig. 9 Conceptual sketch of the isolated propeller flow system, showing the velocity streamlines, the streamtube, and vortex system.

As shown in Fig. 8, the thrust coefficients obtained from the CFD are in good agreement with the experimental data. As the advance ratio J increases, the thrust coefficient C_T shows a parabolic trend with a reduction due to a decrease in the angle of attack of the blade. This behavior arises from the increase of the incoming flow velocity, which alters the relative airflow over the blades, thereby reducing the effective angle of attack and therefore reducing thrust generation efficiency. Furthermore, near the blade tip, the aerodynamic performance diminishes due to the reduced chord length, which lowers the aerodynamic loading and local Reynolds number. This leads to a decrease in aerodynamic efficiency, limiting the thrust contribution of the outer blade sections.

IV. Results and Discussion

To evaluate the impact of aerodynamic interactions on the performance of the propellers in the OAA configuration, we compare the performance of each propeller with that of an isolated one. All propellers were set to operate under the same conditions, with a freestream velocity $V_\infty = 20$ m/s. The thrust and power coefficients for isolated and OAA propellers in the forward and transition phases were evaluated.

A. Isolated Propeller

As the propeller rotates at a given rotational speed n, its blades interact with the air, creating a pressure difference between the upstream (low-pressure) side and the downstream (high-pressure) side. This pressure difference results in accelerated airflow behind the propeller, generating its slipstream [34]. These effects collectively produce the thrust force, which acts perpendicular to the plane of rotation, propelling the aircraft. The slipstream, illustrated in Fig. 9, comprises axial and rotational velocity components and includes a vortex system characterized by tip and root vortices that induce additional velocity components. According to momentum theory [35], the axial velocity increases, leading to a contraction of the streamtube due to mass flow conservation. The slipstream dynamics and their impact on thrust are fundamental to propeller performance analysis.

Figure 10 presents the performance characteristics of the propeller in isolated conditions, highlighting thrust and power coefficients. The thrust coefficients are compared to the experimental data from Stokkermans et al. [18]. The comparison reveals a small difference between the experimental and current CFD predictions. Specifically, the CFD results slightly underestimate the thrust coefficient relative to the experimental measurements. Despite this discrepancy, the overall CFD results and its trend align well with the experimental data, suggesting that the numerical approach captures the key aerodynamic behavior of the propeller. As detailed in Sec. III, the thrust coefficient decreases with increasing advance ratio, consistent with established propeller performance principles. The power coefficient curve also decreases with an increasing advance ratio, reflecting the reduced power requirements at higher rotational speeds for a given forward velocity.

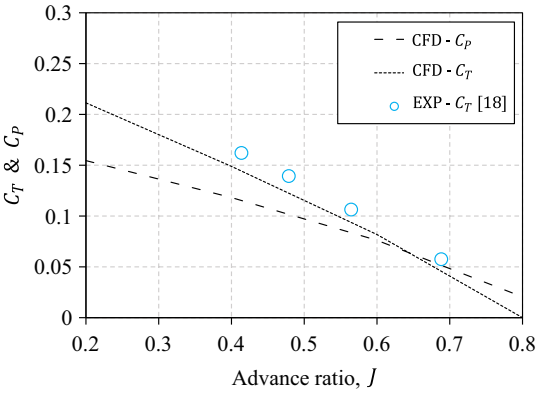

Fig. 10 Isolated propeller performance at $\alpha_p = 0°$, $V_\infty = 20$ m/s: CFD C_T and C_P with experimental C_T from Stokkermans et al. [18].

B. Forward Flight Phase

Two propellers arranged in an OAA configuration with partial overlap are oriented such that their axes of rotation are parallel to the incoming freestream velocity ($\alpha_p = 0°$), representing the forward flight condition (see Fig. 3b). Both propellers are corotating, meaning that they rotate in the same direction relative to their axes. This configuration introduces aerodynamic interactions between the wake of the front propeller and the inflow region of the rear propeller, influenced by the partial overlap. Analysis of this interaction is critical to understanding the effects on thrust generation and efficiency during forward flight.

1. *Performance Analysis*

Figure 11 illustrates a conceptual representation of the flowfield generated by the two corotating OAA propellers. In this configuration, the upstream (front) propeller generates thrust while producing a helical slipstream characterized by axial and rotational velocity components. The downstream (rear) propeller operates within the wake of the front propeller, encountering a nonuniform and distorted inflow. This flow interaction induces unsteady aerodynamic effects that influence the aerodynamic performance, including thrust and efficiency, of the rear propeller.

The performance metrics of the front and rear propellers, as well as an isolated propeller, are shown in Fig. 12 as a function of J.

The predicted thrust ($C_{T,\text{front}}$) and power ($C_{P,\text{front}}$) coefficients of the front propeller showed negligible difference compared to the isolated propeller thrust ($C_{T,\text{iso}}$) and power ($C_{P,\text{iso}}$) coefficients across the entire range of advance ratios analyzed in this study. This outcome is physically understandable, as the front propeller operates in a uniform and undisturbed inflow, thereby experiencing aerodynamic conditions similar to those of an isolated propeller.

On the other hand, the slipstream generated by the front propeller increases the axial velocity of the inflow to certain regions of the rear propeller. This results in an increase in the effective advance ratio experienced by the rear propeller, leading to a reduction in its thrust ($C_{T,\text{rear}}$) and power ($C_{P,\text{rear}}$) coefficients. The merging of the two propeller flows and the increase in axial velocity are conceptually illustrated in Fig. 11.

As shown in Fig. 12a, the thrust coefficient of the rear propeller, $C_{T,\text{rear}}$, remains consistently lower than that of the front propeller, $C_{T,\text{front}}$, across the entire range of advance ratios investigated. This performance reduction arises from aerodynamic interaction caused by the wake of the front propeller, which imposes a nonuniform, accelerated inflow on the rear propeller, reducing the effective thrust generation capability of the rear propeller. The decrease in performance is most pronounced at the lowest advance ratio ($J = 0.2$), where the thrust coefficient drops by 24.26% compared to the front propeller. At $J = 0.4$, the loss reduces slightly to 20.82%. These values are in good agreement with previously reported numerical and experimental studies. For instance, Piccinini et al. [24], Stokkermans et al. [18], and Zanotti et al. [36] reported thrust losses ranging from approximately 6–26% for similar lateral spacing of $d_y = R_p$, depending on the propeller geometry, longitudinal spacing d_x, and advance ratio J.

As J increases, the influence of aerodynamic interaction diminishes progressively, as the wake of the front propeller becomes less dominant in the inflow region of the rear propeller. A similar trend is observed for the power coefficient of the rear propeller, $C_{P,\text{rear}}$, illustrated in Fig. 12b, where the maximum loss of 20.61% is reached at $J = 0.2$. It is important to highlight that the variation in performance loss with respect to J is not linear, as detailed in Table 3, a behavior that was also noted by Zanotti et al. [36] in their experimental works.

Table 3 Losses of thrust ΔC_T and power ΔC_P coefficients of the rear propeller with respect to the front propeller

J	0.2	0.4	0.6
ΔC_T [%]	24.26	20.82	16.15
ΔC_P [%]	20.61	16.93	14.16

The observed decrease in losses with increasing advance ratio between 0.2 and 0.6 is due to the reduced intensity of wake-induced velocity fluctuations and a relative improvement in the rear propeller inflow at higher J. At low J, the axial velocity is small compared to the rotational speed (nD_p), resulting in a high blade loading and angle of attack. Under this condition, the front propeller generates a high-turbulent, momentum-deficient wake with strong swirl components. As J increases (n decreases since V_∞ is constant in this study), the axial velocity component dominates over the rotational effect, reducing the load of the blade and angle of attack. The wake deficit generated by the front propeller is therefore less, reducing its adverse impact on the inflow conditions of the rear propeller.

2. *Flowfield Analysis*

At 50% blade radial position, the pressure coefficient (C_p) was evaluated for the front and rear propeller blades, considering three distinct sections: two outside and one within the overlap region (see Fig. 13). A close view of the blade sections is illustrated in Fig. 14.

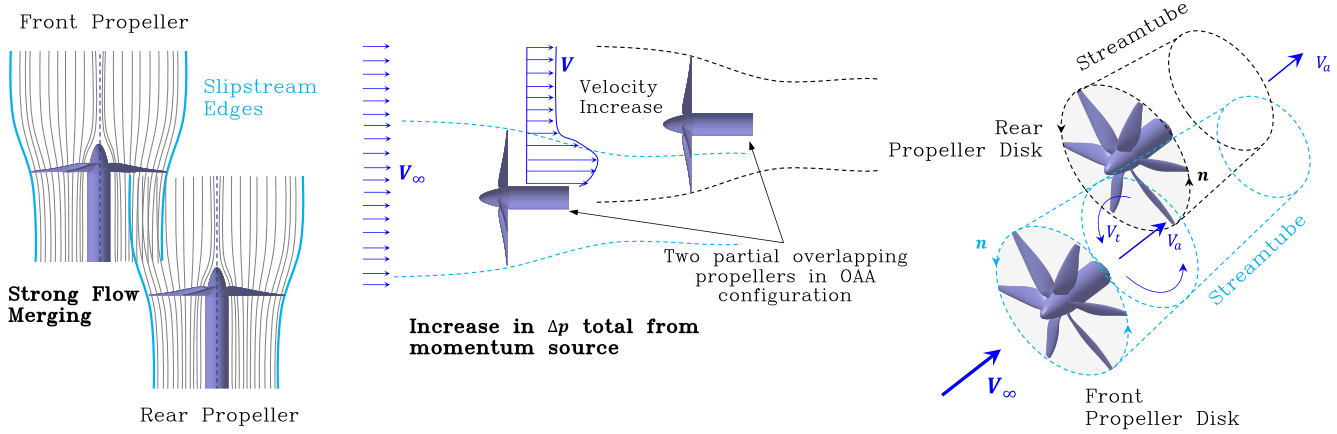

Fig. 11 Conceptual sketch of multirotor flow system of two propellers in OAA configuration, showing partial overlapping and streamtubes interaction.

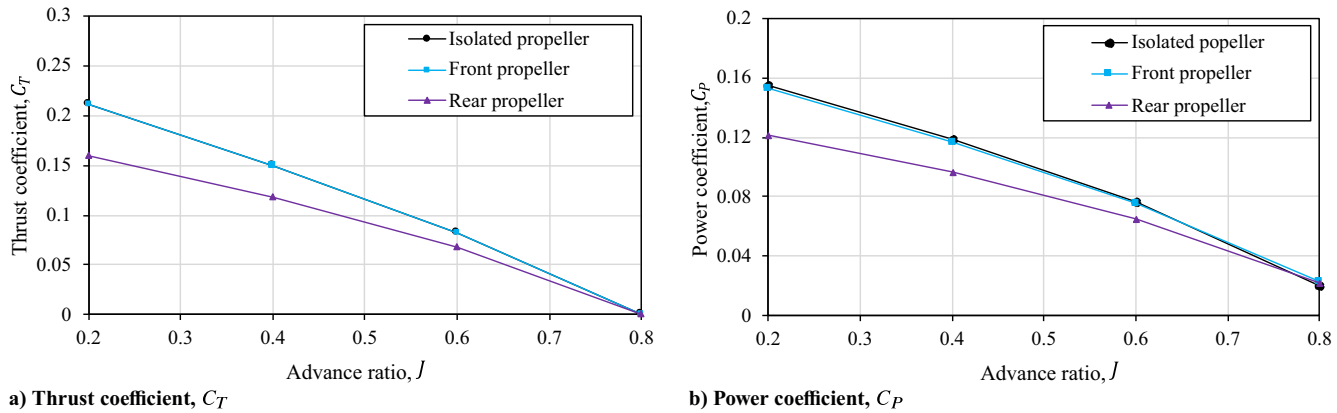

a) Thrust coefficient, C_T **b) Power coefficient, C_P**

Fig. 12 Comparison of the front and rear propellers performances for different advance ratios at $\alpha_p = 0°$.

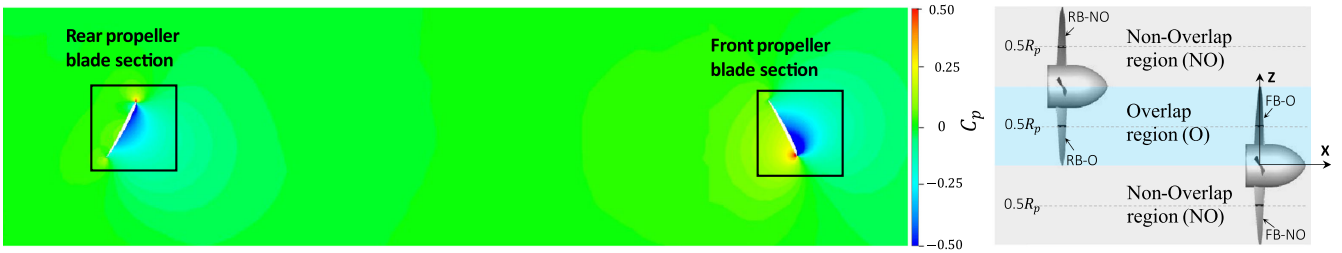

Fig. 13 C_p distribution at $r = 0.5R_p$ blade section within the overlap region for $J = 0.4$ and definition of the regions and the blade nominations.

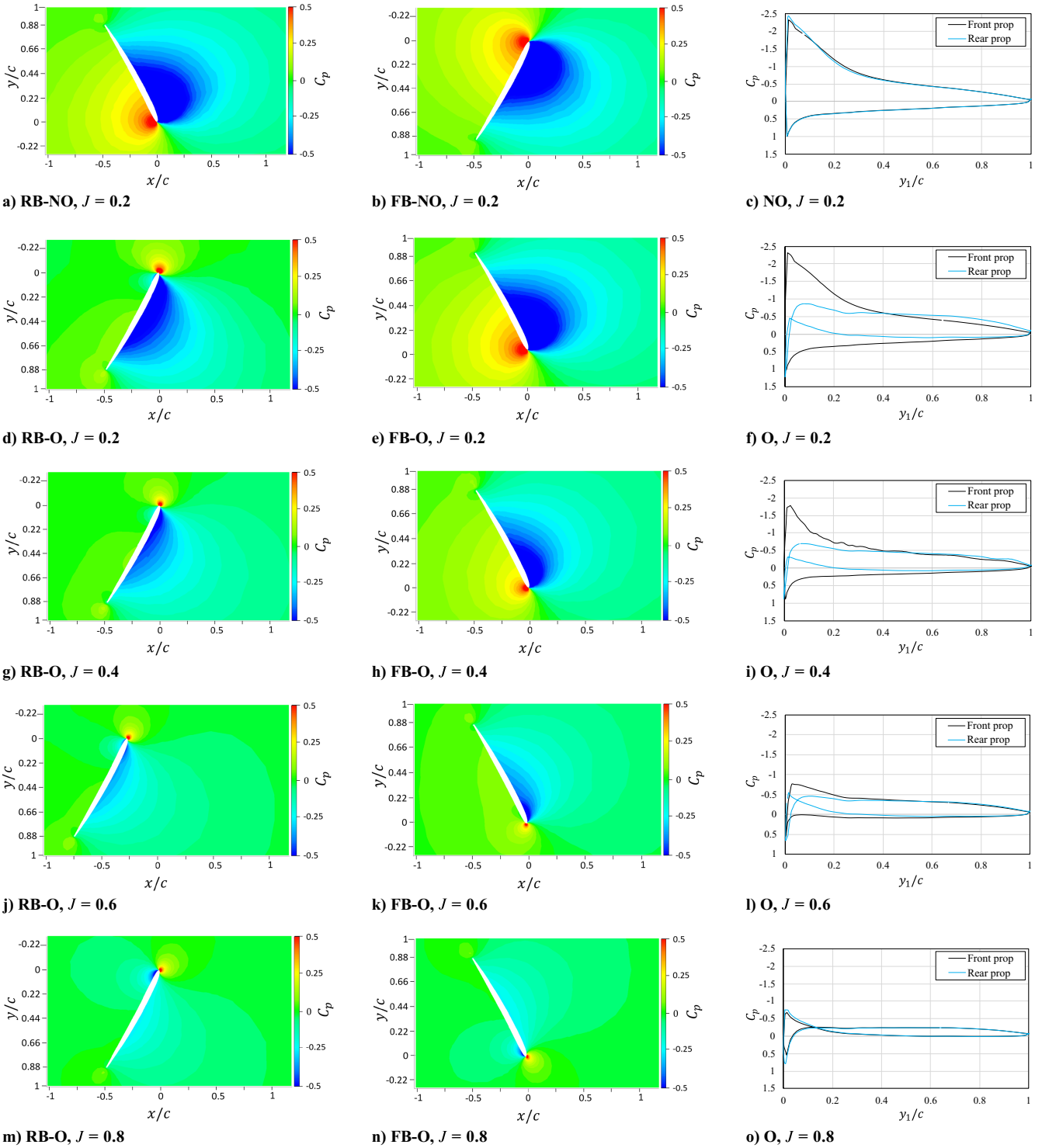

a) RB-NO, $J = 0.2$ **b) FB-NO, $J = 0.2$** **c) NO, $J = 0.2$**

d) RB-O, $J = 0.2$ **e) FB-O, $J = 0.2$** **f) O, $J = 0.2$**

g) RB-O, $J = 0.4$ **h) FB-O, $J = 0.4$** **i) O, $J = 0.4$**

j) RB-O, $J = 0.6$ **k) FB-O, $J = 0.6$** **l) O, $J = 0.6$**

m) RB-O, $J = 0.8$ **n) FB-O, $J = 0.8$** **o) O, $J = 0.8$**

Fig. 14 Comparison of surface C_p at $r = 0.5R_p$ radial position for the rear and front blade sections: a–c) outside the overlap region, and b–o) within the overlap region.

Figures 14a and 14b show the C_p distribution at the blade section in the non-overlap region at $J = 0.2$. Both the rear (RB-NO) and front (FB-NO) blades show identical pressure distributions, and there is a pronounced suction on the upper surface near the leading edge (LE), with a rapid increase in C_p, while the pressure side shows a decrease. The lower surface maintains a relatively uniform C_p except at the LE, as shown by the comparison in Fig. 14c at $J = 0.2$, where we can observe a convergence between the upper and lower surface pressure.

Conversely, in the overlap region, the C_p distribution of the rear (RB-O) and front (FB-O) blades differs noticeably, and this as the advance ratio varies, as depicted in Figs. 14d, 14e, 14g, 14h, 14j, 14k, 14m, and 14n. With increasing J, the intensity of the suction peak increases. The FB-O shows a sharper pressure gradient at the LE compared to the RB-O except at $J = 0.8$, where their profiles converge, with the negative pressure zone shifting toward the lower side near the LE.

For each C_p contour, an associated profile is plotted for the FB-O and RB-O in Figs. 14f, 14i, 14l, and 14o. For advance ratios of 0.2, 0.4, and 0.6, the upper surface of both blades shows a strong suction peak near the LE, followed by a gradual recovery in pressure toward the TE that indicates boundary-layer reattachment. Notably, the C_p profile of the FB-O displays a relatively smooth recovery marked by a distinct plateau or slight dip just after the suction peak. This feature is indicative of a laminar separation bubble (LSB), wherein the laminar boundary layer separates, forms a recirculating region, and subsequently reattaches further downstream. In contrast, the RB-O shows more gradual recovery, suggesting an extended separation region due to wake turbulence, which delays reattachment. The area under the C_p curves of the rear propeller is less compared to the front, specifically 40% at $J = 0.4$ except at $J = 0.8$. At this advance ratio, the areas under the C_p curves of the front and rear propeller blades (see Fig. 14o) are the same and close to zero, highlighting why C_T also approaches zero at this advance ratio, as observed in Fig. 12. This occurs because the propeller operates within a condition where the inflow velocity is high relative to the rotational speed, significantly reducing the effective angle of attack of the blades. When the angle of attack drops below a critical limit, the blades generate minimal lift, resulting in near-zero thrust production. The effects of the advance ratio and the interaction are further highlighted in the plot in Fig. 15 for the C_p for different J.

Figure 16 illustrates the in-plane velocity magnitude distribution within the wake of the two propellers at an advance ratio of $J = 0.4$. Significant flow interaction can be observed near the rear propeller blade, where the incoming flow has been accelerated by the front propeller. This results in an increased local advance ratio and reduced relative velocity difference acting on the rear propeller, which, according to the principles of thrust generation, depends on an available momentum. Since the reduced velocity difference leads to a lower change in momentum, the rear propeller experiences a reduced thrust output.

Additionally, the interaction between the two propellers distorts the wake from a purely circular formation, which would be typical for a single propeller, to a more complex, noncircular shape.

Figure 17 further shows the wake geometry at $J = 0.4$ for various streamwise positions within the planes of the two propellers and at a distance of $0.5R_p$ behind each blade. Before the rear propeller ($x = 0.5R_p$), the slipstream maintains a circular shape, with a uniform velocity distribution over the propeller disk. However, downstream of the rear propeller ($x = 3R_p$), the circular geometry is lost, and the wake shows a merged structure characterized by a high-velocity core in the projected disks' intersection zone. This indicates a nonuniform velocity distribution across the propeller disk, leading to uneven loading over the propeller disk.

The axial velocity distribution profile in the slipstream of the two propellers is illustrated in Fig. 18, which shows the two streamwise positions behind each propeller. Figures 18a and 18b compare the

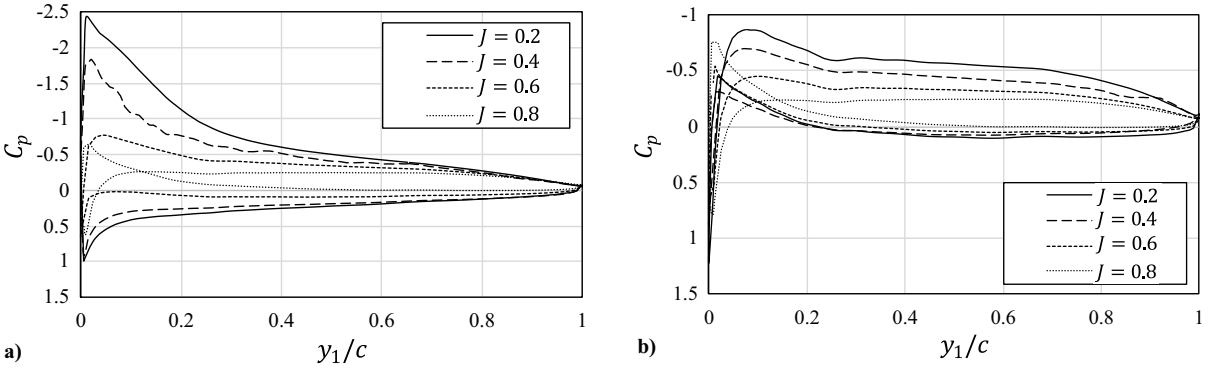

Fig. 15 Pressure coefficient profiles of the rear propeller blades at $r = 0.5R_p$ section for different advance ratios: a) outside overlap region and b) within overlap region.

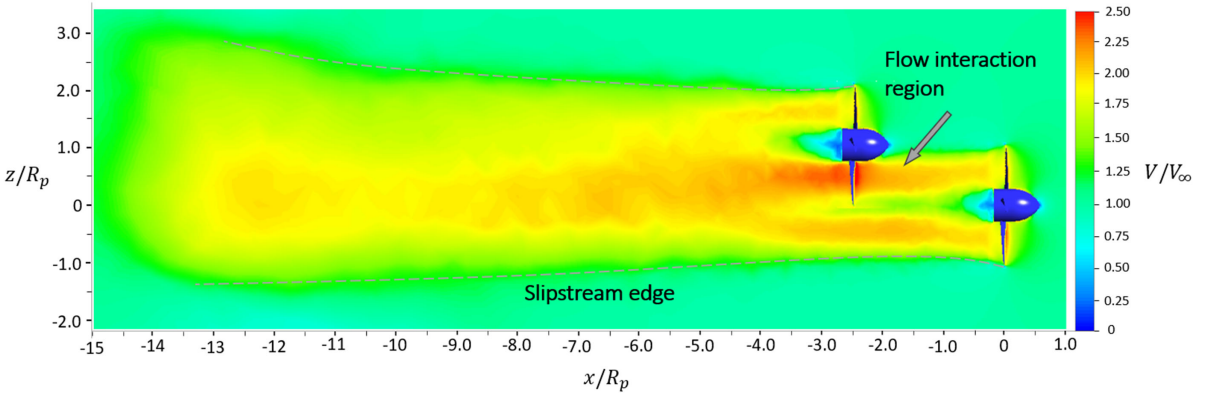

Fig. 16 Velocity magnitude distribution on propellers wake plane (X–Z plane) for $\alpha_p = 0°$ and $J = 0.4$.

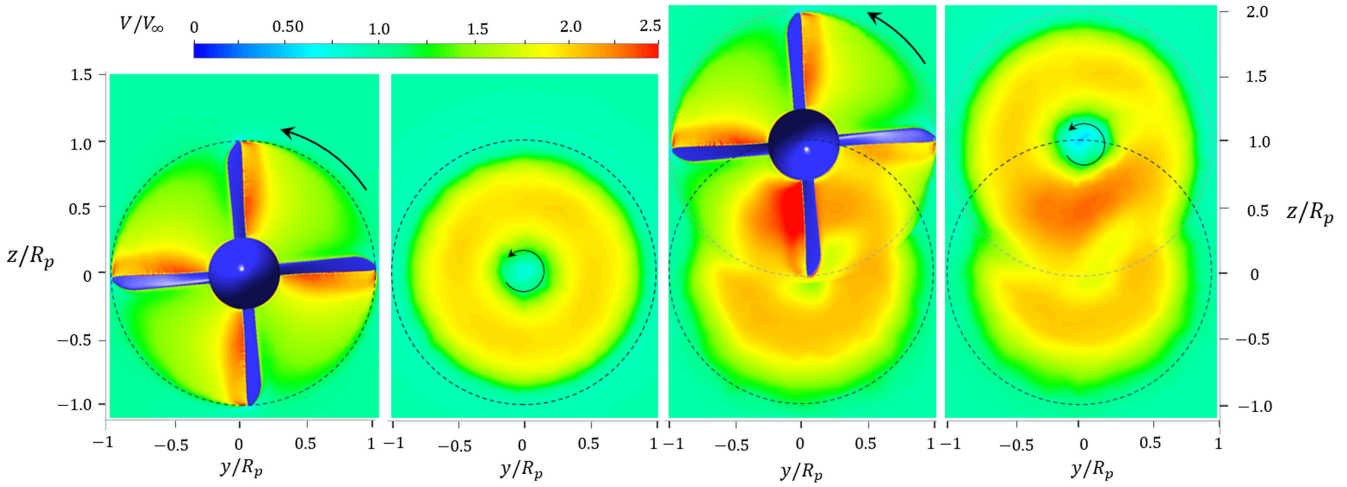

Fig. 17 Velocity magnitude distribution at different streamwise positions for $\alpha_p = 0°$ and $J = 0.4$.

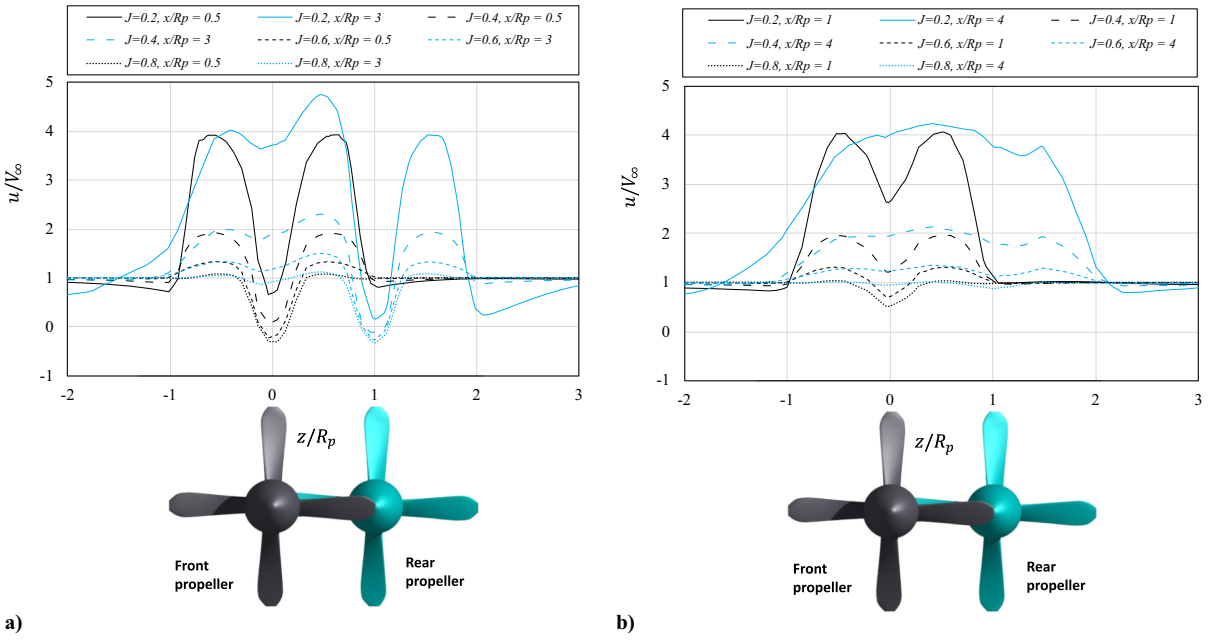

Fig. 18 Axial velocity profile at different streamwise locations and J: a) $0.5R_p$ behind the front ($x/R_p = 0.5$) and the rear ($x/R_p = 3$) propellers, and b) R_p behind the front ($x/R_p = 1$) and the rear ($x/R_p = 4$) propellers.

axial velocity at $x/R_p = 0.5$ and $x/R_p = 1$, respectively, behind each propeller for all the studied advance ratios.

The axial velocity u distribution immediately downstream of the front propeller reveals a remarkable acceleration relative to the freestream velocity V_∞. This acceleration is consistent with the momentum transfer induced by the front propeller, which accelerates the fluid within its immediate slipstream (see Fig. 18a). The high-speed core, concentrated at midspan where the aerodynamic loading is maximal, diminishes toward both the blade tips and the hub. The reduced velocities near these regions can be attributed to the mixing with the ambient air and hub-induced flow blockage. The regions associated with the hub (positions $z/R_p = 0$ and $z/R_p = 1$) display lower velocities, an effect that is attenuated further downstream as the flow gradually homogenizes.

The radial profile of u at the stations upstream of the rear propeller shows symmetry with respect to the rotational axis of the front propeller. The peak values of u decrease with increasing advance ratio J. At a low advance ratio ($J = 0.2$, corresponding to a high rotational speed), the propeller imparts substantial aerodynamic loading, resulting in u significantly exceeding V_∞. In contrast, at higher advance ratios, the ratio u/V_∞ approaches 1, indicating a lower addition of momentum.

Downstream of the rear propeller (streamwise positions $x = 3R_p$ and $x = 4R_p$), the flow is further accelerated, although the increase is less pronounced than that observed immediately behind the front propeller. The peak u values in this region are observed between the radial positions corresponding to the origins of the front ($z/R_p = 0$) and rear ($z/R_p = 1$) propellers. For example, at $J = 0.2$, the peak u/V_∞ measured at $x = 0.5R_p$ behind the front propeller is approximately 3.9, while at $x = 3R_p$ behind the rear propeller it increases to about 4.75, an improvement of roughly 21.8%. A similar percentage increase is observed at $J = 0.4$. Furthermore, the axial velocity distribution across the rear propeller disk shows nonuniformity and asymmetry, primarily due to the localized acceleration acting on only the overlapping part of the disk.

Figure 19 illustrates the vorticity distribution of the two OAA propellers for $J = 0.4$, highlighting both trailing-edge (TE) and tip vortices. For the forward propeller, the tip vortices are clearly visible. In contrast, for the rear propeller, tip vortices only appear on the blade outside the overlap region. Within the overlap region,

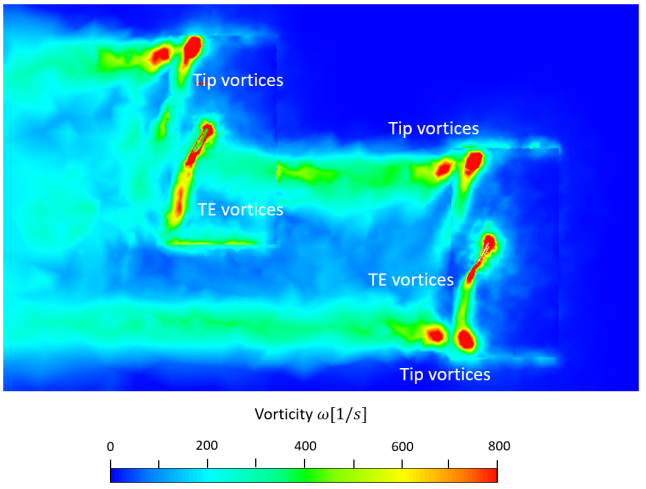

Fig. 19 Vortex field of the two OAA propellers in *X–Z* plane at the position $y = 0.5R_p$, $\alpha_p = 0°$, and $J = 0.4$.

the tip vortices of the rear blade are disrupted, and the helical structure is broken in the chosen display range. This disruption is attributed to the accelerated inflow, which reduces the energy needed for the complete vortex roll-up phase at the tip of the rear blade. As a result, the flow does not have sufficient momentum to move from the higher-pressure side of the blade around the tip to the lower-pressure side, preventing the formation of a strong vortex. Additionally, weaker TE vortices are shed from each blade, which, although showing a lower vorticity than the tip vortices, remain clearly identifiable in the flowfield.

C. Transition Flight Phase

During the transition flight, the propeller tilt angle changes from $\alpha_p = 0°$ (horizontal flight) to $\alpha_p = 90°$ (vertical flight) through the intermediate angles of $\alpha_p = 30°$ and $\alpha_p = 60°$. In this phase, the rotor must simultaneously generate the lift force (vertical component of the thrust) and forward force (horizontal component of the thrust). The thrust components can be expressed as

$$T_v = T\sin(\alpha_p) \Rightarrow C_{T_v} = C_T\sin(\alpha_p) \quad \text{(lift force)} \tag{7}$$

$$T_h = T\cos(\alpha_p) \Rightarrow C_{T_h} = C_T\cos(\alpha_p) \quad \text{(forward force)} \tag{8}$$

Here, C_{T_v} and C_{T_h} represent the vertical and horizontal components, respectively. In this phase, the flow dynamics differ from that in the forward phase, with performance varying based on the propeller angle. Since the front propeller operates in an undisturbed stream, its performance is suggested to be identical to that of an isolated single propeller, as shown for the forward phase in Sec. IV.B. This section focuses on comparing the performance of the rear propeller with that of the front propeller.

1. *Performance Analysis*

Performance of the propellers during the transition phase varies with the tilt angle due to the requirement of the propeller to generate the lift and forward force components. Figure 20 shows the C_T and C_P of the front and rear propellers versus advance ratio for different propeller angles. The curves indicate that for lower tilt angles, specifically $\alpha_p = 30°$ and $\alpha_p = 60°$, both C_T and C_P decrease with increasing J. In these configurations, the rotor operates in a more propeller-dominated flow. As J increases (n decreases since $V = 20$ m/s, a constant), the effective angle of attack of the blades decreases. This reduction in

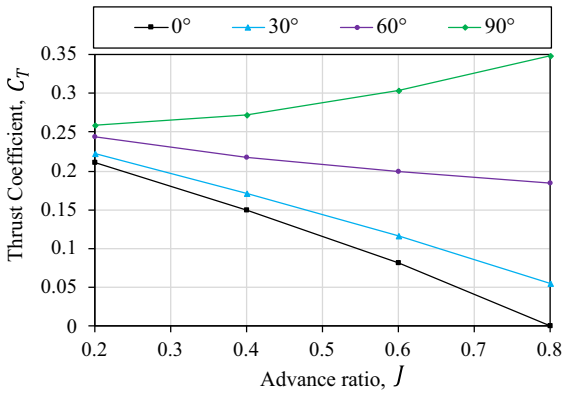

a) Front propeller C_T

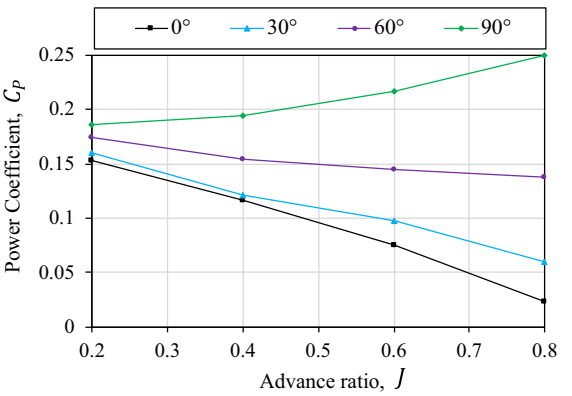

b) Front propeller C_P

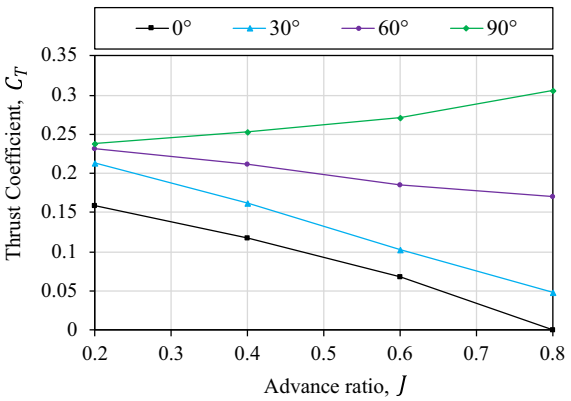

c) Rear propeller C_T

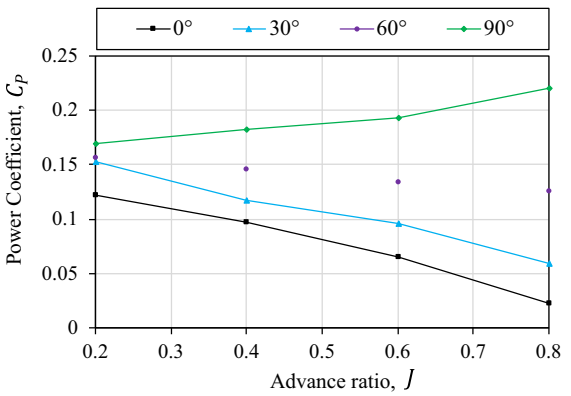

d) Rear propeller C_P

Fig. 20 Thrust and power coefficients of the rear and front propellers versus J for different α_p.

effective angle of attack (AoA) leads to lower C_T and C_P. Notably, the rate of decrease in these coefficients is more pronounced for $\alpha_p = 0°$ and $\alpha_p = 30°$ than $\alpha_p = 60°$, for instance, the difference in front propeller highest and lowest C_T (at $J = 0.2$ and $J = 0.8$, respectively) at $\alpha_p = 30°$ is 0.1658 but only 0.0596 at $\alpha_p = 60°$.

In contrast, when α_p is increased to 90°, the rotor operates in helicopter-like edgewise flow, and the aerodynamic behavior reverses. In this vertical configuration, the rotor blades are oriented to generate lift. As J increases, the relative velocity of the blade shifts from the rotational to axial component. This shift reduces the induced velocity on the advancing blades part, effectively increasing their local angle of attack and dynamic pressure compared to the blades near the azimuthal angle $\Psi = 180°$, which operate at a less effective velocity. As a result, both C_T and C_P increase with J as the blade operates at higher loadings to sustain the necessary lift. The overall trends are consistent with the findings reported by Zanotti et al. [30]. Furthermore, it is worth noting a noticeable fluctuation was observed in the thrust and power coefficients of the two propellers at nonzero tilt angles.

Figure 21 presents the decomposed thrust vector components for propeller tilt angles of 30° and 60°. At a 30° tilt angle (see Fig. 21a), the horizontal component (actual thrust) predominates over the vertical component (lift force). In contrast, at a 60° tilt angle (see Fig. 21b), the vertical component exceeds the horizontal component.

Figure 22 illustrates the comparison between the performance of the front and rear propellers as the tilt angle increases from 0° to 90°. In this study, particular attention was paid to the evaluation of the interactions and aerodynamic performance of the rear propeller relative to the front one. For lower tilt angles ($\alpha_p = 0°$), the aerodynamic interaction between the propellers is more pronounced due to a larger overlapping region in the flowfield, resulting in a noticeable performance gap between the two units. As the tilt angle increases to 30° and further to 60°, the effective overlap between the propellers decreases. At 30°, C_T and C_P of the rear propeller approach those of the front propeller, although a nonzero overlapping region still exists. In contrast, at 60° tilt, the overlapping zone becomes negligible, eliminating aerodynamic interference; consequently, the performance curves of the two propellers converge. Overall, as the tilt angle increases, C_T and C_P increases as well.

As the tilt angle increases, the rotor must generate significant vertical lift to support the aircraft weight. This transition requires the blades to operate at higher effective angles of attack to produce the needed lift, which in turn increases the aerodynamic loading. The increase in blade loading increases the induced velocity and associated induced drag, which requires more power input. Consequently, C_T and C_P increase. Moreover, as the rotor tilts more vertically, the interaction effects within the rotor wake and the interaction between the incoming freestream and the rotational-induced flow become more complex, further raising the thrust and power.

Table 4 presents the differences in C_T and C_P between the rear and front propellers across various advance ratios. For all the considered J, the thrust discrepancy is more pronounced at a 30° transition angle than at 60°, confirming that the interaction effects persist when the geometric overlap is nonzero. In particular, at an advance ratio of $J = 0.2$, the difference in $C_T(\Delta C_T)$ is slightly lower at 30° compared to 60°. In contrast, the difference in C_P (ΔC_P) is higher at 60°; this is attributed to the increased induced drag associated with higher tilt angles, which in turn requires greater torque and results in a higher power coefficient. Overall, while the rear propeller generally shows lower performance than the front propeller, the diminishing interaction with an increased tilt angle leads to a convergence of their performance characteristics.

At a 30° tilt angle, as J increases, the difference in the C_P between the front and rear propellers (ΔC_P) decreases monotonically. This indicates that, with increasing J, the aerodynamic power requirements of the two propellers become similar. In contrast, the ΔC_T follows an opposite trend at 30°, increasing until a 0.6 advance ratio and decreasing at 0.8. At 60°, the behavior of ΔC_P is more complex. Initially, as J increases from 0.2 to 0.4, ΔC_P decreases. However, as J increases further from 0.4 to 0.8, ΔC_P begins to increase again, although its value at $J = 0.8$ remains lower than at $J = 0.2$. This non-monotonic behavior is the same for ΔC_T, which results from a complex flow at higher α_p and the changes in the effective blade angle of attack, and the corresponding variations in induced velocity profiles as the rotor shifts toward a vertical flow regime.

2. *Flow Analysis*

To elucidate the aerodynamic interactions in the OAA configuration during the transition phase, wake characteristics were examined at a typical advance ratio, $J = 0.4$, for propeller tilt angles of 30°, 60°, and 90°. Figure 23 presents the velocity magnitude contours in the X–Z plane. In all transition angles, both the front and rear propeller wakes show noticeable deflection. This deflection results from the combination of the rotational motion of the propeller, which tends to force the air downward, and the lateral momentum of the incoming freestream, which shifts the slipstream toward the flow direction. In addition, the velocity immediately below the advancing blades is significantly higher than that below the retreating blades for both propellers, indicating a nonuniform loading across the propeller disks when nonzero tilt angles are applied.

As seen in Fig. 23a, the deflected airflow from the front propeller impinges on the rear propeller, particularly on its advancing blades side, which locally increases the effective advance ratio. This interaction causes the reduction in performance of the rear propeller relative to the front one, as observed in Fig. 20. With increasing tilt angle, the extent of direct impingement on the rear propeller is diminished; however, the deflection of the front propeller inflow causes the rear propeller to receive a partially deflected stream. This deflection explains why even under reduced interaction conditions the rear propeller still develops lower thrust and power compared to the front propeller.

At a tilt angle of 90° (Fig. 23c), the propellers operate in an edgewise flow regime, resembling the forward flight condition of conventional helicopters. This orientation induces asymmetric inflow over the rotor disk, with advancing blades experiencing

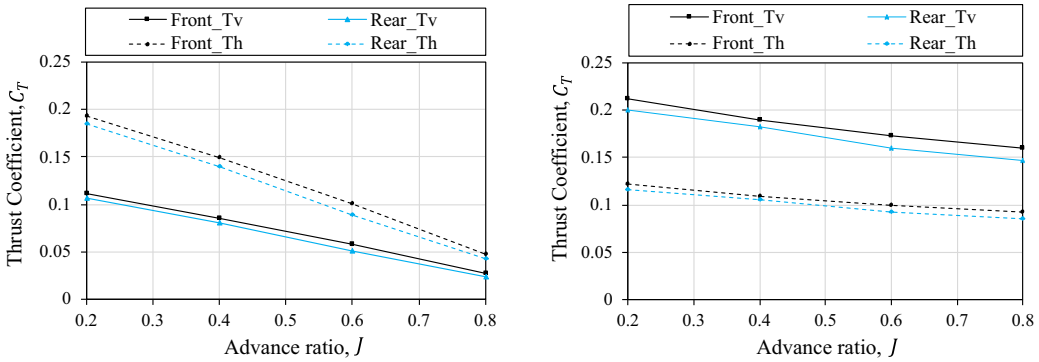

a) α_p **= 30°** **b)** α_p **= 60°**

Fig. 21 Horizontal and vertical components of the thrust coefficients.

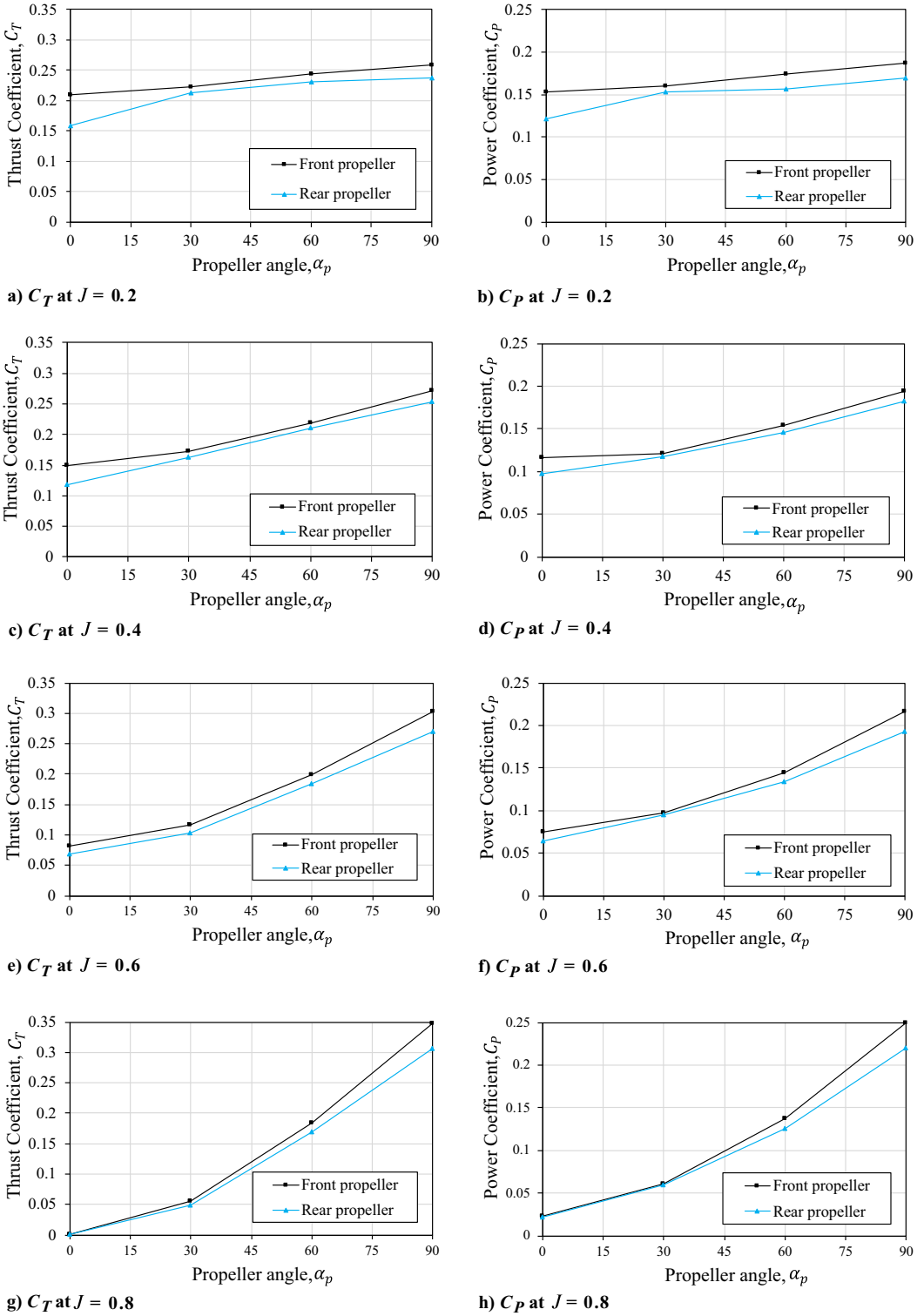

Fig. 22 Comparison of thrust and power coefficients at different α_p and J.

Table 4 Rear propeller performance loss with respect to front propeller at 30° and 60° tilt angles

	$\alpha_p = 30°$		$\alpha_p = 60°$	
J	ΔC_T, %	ΔC_P, %	ΔC_T, %	ΔC_P, %
0.2	4.27	4.19	5.32	10.13
0.4	5.79	3.16	3.38	5.03
0.6	11.11	2.17	7.45	7.18
0.8	10.76	1.0	8.14	8.42

higher relative velocities than retreating blades, a phenomenon known as dissymmetry of lift in traditional helicopters, as observed by Misiorowski et al. [37]. However, since the freestream does not impinge directly on the propeller disks, the effective angle of attack improves, resulting in increased lift and consequently higher thrust. This behavior contrasts with conventional forward flight, where an increase in advance ratio typically leads to a reduction in thrust.

The difference between the advancing and retreating parts of both the front and rear propellers is further illustrated in Figs. 24–26, with the velocity magnitude in the planes parallel to the propeller plane, taken in different positions downstream. At a tilt angle of 30°,

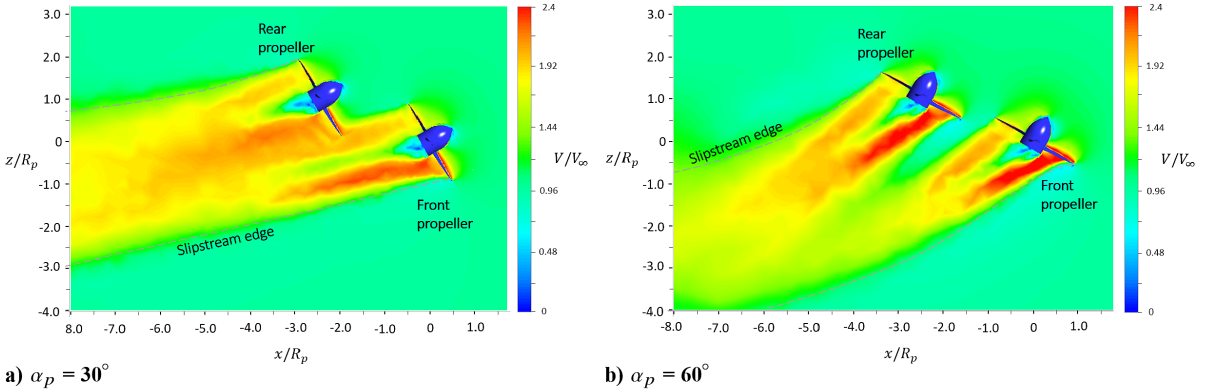

a) $\alpha_p = 30^\circ$ **b)** $\alpha_p = 60^\circ$

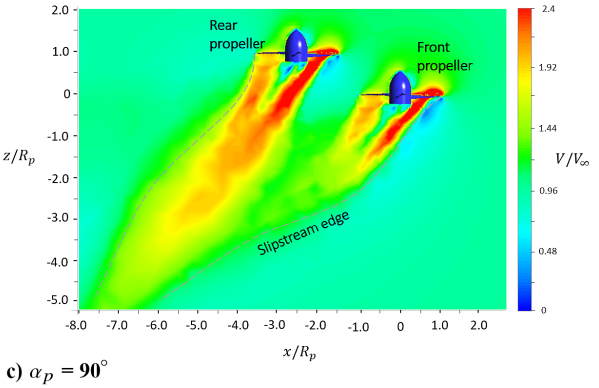

c) $\alpha_p = 90^\circ$

Fig. 23 Velocity magnitude distribution on propellers wake plane (X–Z plane) at $J = 0.4$.

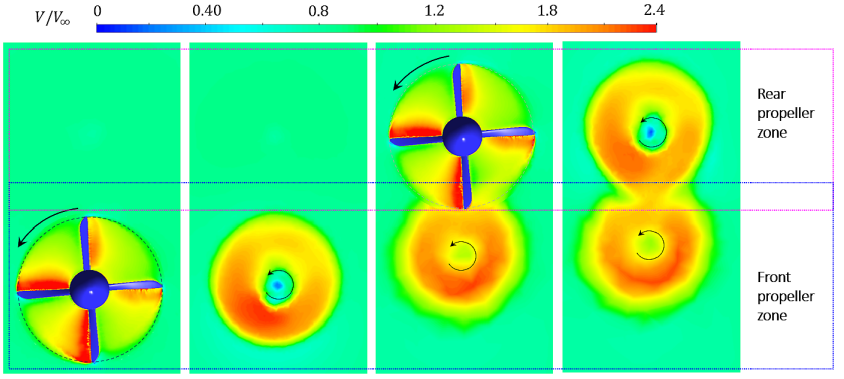

a) $x/R_p = 0$ **b)** $x/R_p = -0.5$ **c)** $x/R_p = -2.5$ **d)** $x/R_p = -3$

Fig. 24 Velocity magnitude in downstream planes parallel to propeller plane for OAA propellers at $\alpha_p = 30^\circ$ and $J = 0.4$.

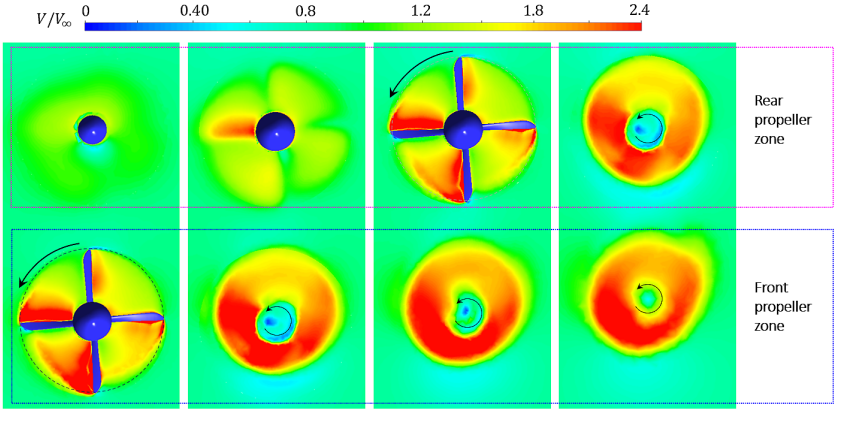

a) $x/R_p = 0$ **b)** $x/R_p = -0.5$ **c)** $x/R_p = -2.5$ **d)** $x/R_p = -3$

Fig. 25 Velocity magnitude in downstream planes parallel to propeller plane for OAA propellers at $\alpha_p = 60^\circ$ and $J = 0.4$.

Figs. 24a and 24b reveal high-velocity regions concentrated in the lower sections of the measurement planes upstream of the rear propeller. Positioned at approximately $(x/R_p = 2.5, z/R_p = 1)$, the rear propeller disk clearly shows evidence of interaction with the incoming flow from the front propeller (see Figs. 24c and 24d). In general, the circular geometry of the wake sections is maintained downstream, except where strong interaction effects are present. However, for the $\alpha_p = 60°$, as shown in Fig. 25, the flow interaction is absent. Although the high-velocity region associated with the advancing blades remains distinct, the circular shape of the streamtube progressively deteriorates downstream. A more concentrated destruction in the streamtube is observed for the 90° tilt due to the edgewise flow, as shown in Fig. 26.

At these nonzero tilt angles and at an advance ratio of $J = 0.4$, the vortex field is analyzed, and it shows pronounced deflection in the freestream direction, as shown in Fig. 27. This deflection arises primarily from the interaction between the propeller-induced downwash and the lateral momentum of the incoming airflow. Consequently, well-defined tip vortices form behind both the front and rear propellers in regions where the wakes either partially overlap or not. This behavior contrasts with that observed in the forward flight configuration (see Fig. 19), where the overlapping region suppresses the helical formation of distinct tip vortices on the overlapping blades' tips.

Moreover, as the tilt angle increases from 30° to 60° and further to 90°, the deflected slipstream increasingly alters the local flow conditions around the blades. Notably, the TE vortices, which are initially distinct, begin to merge with the tip vortices from the advancing blade. This merging is attributed to the increase downward of the flow, which modifies the effective angle of attack and local velocity distribution along the blade span. The merging of these vortical structures not only reconfigures the wake geometry but also has significant implications for the loading and performance characteristics of the propellers during the transition phase.

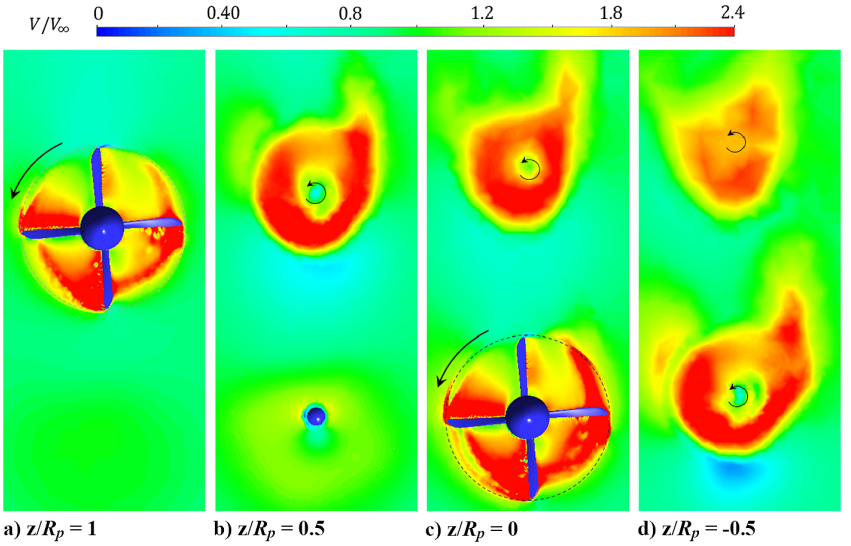

a) $z/R_p = 1$ b) $z/R_p = 0.5$ c) $z/R_p = 0$ d) $z/R_p = -0.5$

Fig. 26 Velocity magnitude in downstream X–Y planes for OAA propellers at $\alpha_p = 90°$ and $J = 0.4$.

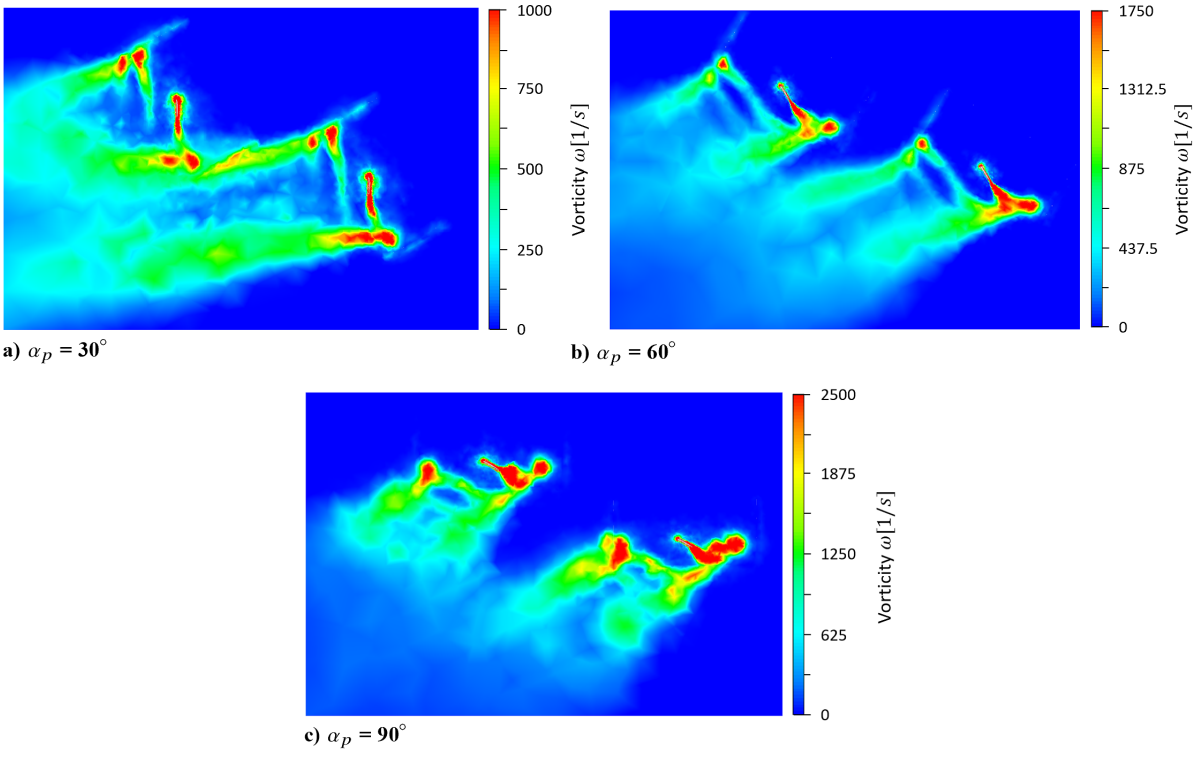

a) $\alpha_p = 30°$ b) $\alpha_p = 60°$

c) $\alpha_p = 90°$

Fig. 27 Vortex field of the two OAA propellers in X–Z plane at the position $y = 0.5R_p$, $\alpha_p \neq 0$, and $J = 0.4$.

V. Conclusions

This study presents a comprehensive numerical investigation of aerodynamic interactions in multirotor configurations during forward and transition flight. The results indicate that in an OAA arrangement, the rear propeller experiences thrust losses of up to 24% in forward flight due to wake impingement from the front propeller. During transition, increased propeller tilt angles reduce geometric overlap and aerodynamic interference, improving rear propeller performance; however, it remains lower than that of the front propeller. Flowfield analysis identifies wake nonuniformity and slipstream deflection as primary contributors to these performance discrepancies. In vertical flight, propellers operate under full edgewise flow conditions similar to those encountered by helicopter rotors, resulting in dissymmetry of lift between advancing and retreating blades. These unsteady aerodynamic phenomena can affect the stability and efficiency of eVTOL vehicles. To mitigate these effects, tiltrotor, tiltwing, and lift-plus-cruise architectures offer potential improvements in aerodynamic efficiency for eVTOL applications by aligning the propeller with the incoming flow. Overall, this work highlights the critical influence of rotor spacing and orientation on propeller aerodynamic performance, emphasizing their importance in the preliminary design of efficient multirotor systems. Future work should include high-fidelity simulations and experimental investigations of multirotor configurations, applying parametric studies of rotor spacing effects on overall vehicle performance. Furthermore, aerodynamic noise generated by propeller interactions in nonaxial inflow conditions requires detailed analysis to support the development of quieter eVTOL designs. Overall, the findings of this study provide a foundation for more detailed investigations aimed at optimizing propulsion configurations in urban air mobility platforms.

Acknowledgments

The authors gratefully acknowledge the Faculty of Aerospace Engineering, Delft University of Technology, for hosting the author Kangni Combey as a visiting Ph.D. researcher and for providing the computational resources and models used in this study. The authors also thank the LERMA Laboratory at the International University of Rabat for their support.

References

[1] Palaia, G., Abu Salem, K., Cipolla, V., Binante, V., and Zanetti, D., "A Conceptual Design Methodology for e-VTOL Aircraft for Urban Air Mobility," *Applied Sciences*, Vol. 11, No. 22, 2021, Paper 10815. https://doi.org/10.3390/app112210815

[2] Polaczyk, N., Trombino, E., Wei, P., and Mitici, M., "A Review of Current Technology and Research in Urban On-Demand Air Mobility Applications," *8th Biennial Autonomous VTOL Technical Meeting and 6th Annual Electric VTOL Symposium*, Vertical Flight Soc. Mea, Arizona, 2019, pp. 333–343, http://resolver.tudelft.nl/uuid:10d1c68a-dfb9-4419-a912-26e6c1742853.

[3] Bauranov, A., and Rakas, J., "Designing Airspace for Urban Air Mobility: A Review of Concepts and Approaches," *Progress in Aerospace Sciences*, Vol. 125, Aug. 2021, Paper 100726. https://doi.org/10.1016/j.paerosci.2021.100726

[4] Fard, M. T., He, J., Huang, H., and Cao, Y., "Aircraft Distributed Electric Propulsion Technologies—A Review," *IEEE Transactions on Transportation Electrification*, Vol. 8, No. 4, 2022, pp. 4067–4090. https://doi.org/10.1109/TTE.2022.3197332

[5] Qu, W., Xu, C., Tan, X., Tang, A., He, H., and Liao, X., "Preliminary Concept of Urban Air Mobility Traffic Rules," *Drones*, Vol. 7, No. 1, 2023, p. 54. https://doi.org/10.3390/drones7010054

[6] Anderson, J. D., *Aircraft Performance and Design*, 1st ed., WCB McGraw-Hill Education, New York, 2010.

[7] Rao, J. P., Holzsager, J. E., Maia, M. M., and Diez, J. F., "Experimental Study into Optimal Configuration and Operation of Two-Four Rotor Coaxial Systems for eVTOL Vehicles," *Aerospace*, Vol. 9, No. 252, 2022, p. 452, https://www.mdpi.com/2226-4310/9/8/452.

[8] Li, J., Sheng, H., Liu, S., Chen, Q., and Zhang, H., "Adaptive Fault-Tolerant Control of Distributed Electric Propulsion Aircraft Based on Multivariable Model Predictive Control," *Expert Systems with Applications*, Vol. 255, Dec. 2024, Paper 124539. https://doi.org/10.1016/j.eswa.2024.124539

[9] Johnson, W., Silva, C., and Solis, E., "Concept Vehicles for VTOL Air Taxi Operations," *AHS Specialists"Conference on Aeromechanics Design for Transformative Vertical Flight*, 2018, https://rb.gy/x55kz7.

[10] Silva, C., Johnson, W. R., Solis, E., Patterson, M. D., and Antcliff, K. R., "VTOL Urban Air Mobility Concept Vehicles for Technology Development, Aviation Technology," *Integration, and Operations Conference*, AIAA Paper 2018-3847, 2018. https://doi.org/10.2514/6.2018-3847

[11] Dingeldein, R. C., *Wind-Tunnel Studies of the Performance of Multirotor Configurations*, Vol. 3236, National Advisory Committee for Aeronautics, NACA-TN-3236, Washington, D.C., 1954, https://ntrs.nasa.gov/citations/19930083899.

[12] Sweet, G. E., *Hovering Measurements for Twin-Rotor Configurations with and Without Overlap*, National Aeronautics and Space Administration, NASA-TN-D-534, Washington, D.C., 1960, https://ntrs.nasa.gov/citations/20040016423.

[13] Ramasamy, M., "Hover Performance Measurements Toward Understanding Aerodynamic Interference in Coaxial, Tandem, and Tilt Rotors," *Journal of the American Helicopter Society*, Vol. 60, No. 3, 2015, pp. 1–17. https://doi.org/10.4050/JAHS.60.032005

[14] Zanotti, A., "Experimental Study of the Aerodynamic Interaction Between Side-by-Side Propellers in Evtol Airplane Mode Through Stereoscopic Particle Image Velocimetry," *Aerospace*, Vol. 8, No. 9, 2021, p. 239. https://doi.org/10.3390/aerospace8090239

[15] Lee, H., and Lee, D.-J., "Rotor Interactional Effects on Aerodynamic and Noise Characteristics of a Small Multirotor Unmanned Aerial Vehicle," *Physics of Fluids*, Vol. 32, No. 4, 2020, Paper 047107. https://doi.org/10.1063/5.0003992

[16] Zhou, W., Ning, Z., Li, H., and Hu, H., "An Experimental Investigation on Rotor-to-Rotor Interactions of Small UAV Propellers," *35th AIAA Applied Aerodynamics Conference*, AIAA Paper 2017-3744, 2017. https://doi.org/10.2514/6.2017-3744

[17] Alvarez, E. J., Schenk, A., Critchfield, T., and Ning, A., "Rotor-On-Rotor Aeroacoustic Interactions of Multirotor in Hover," *Vertical Flight Society's 76th Annual Forum*, The Vertical Flight Soc., Virginia Beach, VA, 2020, pp. 1–12. https://doi.org/10.4050/F-0076-2020-16489

[18] Stokkermans, T. C., Usai, D., Sinnige, T., and Veldhuis, L. L., "Aerodynamic Interaction Effects Between Propellers in Typical eVTOL Vehicle Configurations," *Journal of Aircraft*, Vol. 58, No. 4, 2021, pp. 815–833. https://doi.org/10.2514/1.C035814

[19] Alvarez, E. J., and Ning, A., "High-Fidelity Modeling of Multirotor Aerodynamic Interactions for Aircraft Design," *AIAA Journal*, Vol. 58, No. 10, 2020, pp. 4385–4400. https://doi.org/10.2514/1.J059178

[20] Yoon, S., Lee, H. C., and Pulliam, T. H., "Computational Analysis of Multi-Rotor Flows," *54th AIAA Aerospace Sciences Meeting*, AIAA Paper 2016-0812. 2016. https://doi.org/10.2514/6.2016-0812

[21] Veismann, M., and Gharib, M., "High Fidelity Aerodynamic Force Estimation for Multirotor Crafts in Free Flight," *AIAA SciTech 2020 Forum*, AIAA Paper 2020-0303, 2020. https://doi.org/10.2514/6.2020-0303

[22] de Vries, R., van Arnhem, N., Sinnige, T., Vos, R., and Veldhuis, L. L., "Aerodynamic Interaction Between Propellers of a Distributed-Propulsion System in Forward Flight," *Aerospace Science and Technology*, Vol. 118, Nov. 2021, Paper 107009. https://doi.org/10.1016/j.ast.2021.107009

[23] Gao, Z., Zheng, S., Zhang, S., Wang, H., Shao, X., and Zeng, L., "Aerodynamic Characteristics Study on Multiple Propellers in Distributed Electric Propulsion Configurations," *Physics of Fluids*, Vol. 37, No. 1, Jan. 2025, Paper 0245989. https://doi.org/10.1063/5.0245989

[24] Piccinini, R., Tugnoli, M., and Zanotti, A., "Numerical Investigation of the Rotor-Rotor Aerodynamic Interaction for eVTOL Aircraft Configurations," *Energies*, Vol. 13, No. 22, 2020, p. 5995. https://doi.org/10.3390/en13225995

[25] Combey, K., Elsayed, O. A., Qaissi, K., and Faqir, M., "Numerical Analysis of Multirotor Aerodynamic Interactions in One-After-Another Configuration," *Delft International Conference on Urban Air Mobility 2024 (DICUAM2024)*, TU Delft, Delft, The Netherlands, 2024, https://cdn.aanmelderusercontent.nl/i/doc/31d62a2598dec71be8c2763b4713395f?forcedownload=True.

[26] Qaissi, K., Elsayed, O., Faqir, M., and Essadiqi, E., "Aerodynamic Optimization of Trailing-Edge-Serrations for a Wind Turbine Blade

Using Taguchi Modified Additive Model," *Energies*, Vol. 16, No. 3, 2023, p. 1099.
https://doi.org/10.3390/en16031099

[27] Elsayed, O. A., Asrar, W., and Omar, A. A., "Reverse Delta Wing Trailing Vortex Characteristics by Particle Image Velocimetry (PIV)," *3rd International Symposium on Advanced Fluid/Solid Science and Technology in Experimental Mechanics*, Tainan, Taiwan, 2008.

[28] Elsayed, O. A., Asrar, W., Omar, A. A., and Kwon, K., "Evolution of NACA23012 Wake Vortices Structure Using PIV," *Journal of Aerospace Engineering*, Vol. 25, No. 1, 2012, pp. 10–20.
https://doi.org/10.1061/(ASCE)AS.1943-5525.0000109

[29] Combey, K., Elsayed, O. A., Chouiyakh, H., Qaissi, K., and Faqir, M., "Aerodynamics Investigation of Novel Toroidal Joined Blade Tips Propeller," *Delft International Conference on Urban Air Mobility 2024 (DICUAM2024)*, TU Delft, Delft, The Netherlands, 2024, https://cdn.aanmelderusercontent.nl/i/doc/faa8920ad13bb0a7ba1921c0254c35ed?forcedownload=True.

[30] Zanotti, A., Velo, A., Pepe, C., Savino, A., Grassi, D., and Riccobene, L., "Aerodynamic Interaction Between Tandem Propellers in eVTOL Transition Flight Configurations," *Aerospace Science and Technology*, Vol. 147, April 2024, Paper 109017.
https://doi.org/10.1016/j.ast.2024.109017

[31] ANSYS, *ANSYS Fluent Theory Guide*, Release 12.0 ©ANSYS, Inc., Canonsburg, PA, 2009, https://www.afs.enea.it/project/neptunius/docs/fluent/html/th/node1.htm.

[32] Menter, F. R., "Two-Equation Eddy-Viscosity Turbulence Models for Engineering Applications," *AIAA Journal*, Vol. 32, No. 8, 1994, pp. 1598–1605.
https://doi.org/10.2514/3.12149

[33] Grande, E., Romani, G., Ragni, D., Avallone, F., and Casalino, D., "Aeroacoustic Investigation of a Propeller Operating at Low Reynolds Numbers," *AIAA Journal*, Vol. 60, No. 2, 2022, pp. 860–871.
https://doi.org/10.2514/1.J060611

[34] Anderson, John D., and J, *Fundamentals of Aerodynamics*, 5th ed., McGraw-Hill, New York, 2011.

[35] Froude, W., "On the Elementary Relation Between Pitch, Slip, and Propulsive Efficiency," TR NACA-TM-1, NASA, Washington, D.C., 1920, https://ntrs.nasa.gov/citations/19930080719.

[36] Zanotti, A., and Algarotti, D., "Aerodynamic Interaction Between Tandem Overlapping Propellers in eVTOL Airplane Mode Flight Condition," *Aerospace Science and Technology*, Vol. 124, 2022, Paper 107518.
https://doi.org/10.1016/j.ast.2022.107518

[37] Misiorowski, M., Gandhi, F., and Oberai, A. A., "Computational Study on Rotor Interactional Effects for a Quadcopter in Edgewise Flight," *AIAA Journal*, Vol. 57, No. 12, 2019, pp. 5309–5319.
https://doi.org/10.2514/1.J058369

J. C Hsu
Associate Editor